

---

# 1 An explainable deep learning model based on 2 hydrological principles for flood simulation and 3 forecasting

4 Xin Xiang<sup>1</sup>, Shenglian Guo<sup>1,\*</sup>, Chenglong Li<sup>1</sup>, Yun Wang<sup>2</sup>

5 <sup>1</sup>State Key Laboratory of Water Resources Engineering and Management, Wuhan University, Wuhan, 430072, China

6 <sup>2</sup>Water Resources Technical College, Wuhan, 430072, China

7 Correspondence to: Shenglian Guo (slguo@whu.edu.cn)

8 **Abstract:** Deep learning (DL) models always perform well in hydrological simulation but lack physical-  
9 based principles. To address this gap, we integrate the relatively complex runoff generation and flow  
10 routing principals of Xinanjiang (XAJ) model into the architecture of recurrent neural network (RNN)  
11 units and establish a physical-based XAJRNN layer. Subsequently, this layer is fused with LSTM layers  
12 to construct an explainable deep learning (EDL) model, which underwent testing at the Lushui River and  
13 Qingjiang River basins in China. Compared to benchmark models, the proposed EDL model performs  
14 very well, the average Nash-Sutcliffe efficiency (*NSE*) values for these two basins are 0.98 and 0.94,  
15 respectively. The flood peak relative errors (*PRE*) and peak timing difference ( $\Delta T$ ) are close to zero,  
16 which demonstrate that the EDL model can accurately simulate flood events. Notably, the EDL model  
17 incorporated physical principles not only can improve flow simulation accuracy, but also enhance  
18 interpretability, which offer fresh insights for the fusion of DL and hydrological models for flood  
19 simulation and forecasting.

## 20 1 Introduction

21 In the modern era, flood disasters present substantial threats to both human societies and the natural  
22 environment (Guido et al., 2023). With the intensification of global climate change and rapid  
23 urbanization, the accuracy and timeliness of flood forecasting have become increasingly important. Flood  
24 forecasting typically relies on hydrological models (Thaisiam et al., 2024). By analyzing the rainfall-  
25 runoff relationships from historical periods, hydrological models simulate hydrological processes within

---

26 a basin. Combining these with forecasted rainfall, such models can forecast flow discharges, water levels,  
27 and probabilities of flood occurrence. In recent years, advancements in computational power and  
28 artificial intelligence (AI) technologies have significantly improved the accuracy and real-time  
29 responsiveness of hydrological models (Hirabayashi et al., 2013), offering more scientific and efficient  
30 support for disaster prevention and mitigation efforts.

31 Traditional hydrological models rely on statistical methods and empirical formulas but struggle to  
32 accurately simulate complex nonlinear hydrological processes (Roy et al., 2023). Their predefined  
33 equations are unable to adapt the climate and environmental changes such as land use and human  
34 activities. Additionally, these models often simplify rainfall spatiotemporal distribution and the land  
35 surface heterogeneity. In recent years, deep learning (DL) technologies have made significant  
36 advancements in various fields, particularly in time series prediction, where they display strong potential.  
37 DL, a domain dedicated to uncovering patterns and extracting knowledge from large datasets, enables  
38 computers to autonomously learn algorithms, analyze extensive sample data, and identify patterns,  
39 facilitating predictions on unfamiliar data. This process closely aligns with hydrological modeling, which  
40 discerns patterns by analyzing historical hydrometeorological data, generalizing, and simulating  
41 hydrological processes. Consequently, DL has attracted widespread attention in hydrology (Nearing et  
42 al., 2021).

43 DL commonly refers to deep neural networks, a form of representational learning technique that  
44 links simple nonlinear computational units through multi-layer network architectures to understand  
45 intricate relationships. It falls within the realm of machine learning (ML) (Yann et al., 2015). The term  
46 "deep" in DL signifies network structures with multiple layers and neurons, although there is no precise  
47 definition of "deep". Generally, it denotes models that necessitate substantial data and encompass  
48 numerous layers and neurons. These layers convert their inputs into higher-level features, magnifying  
49 crucial factors for output variability while reducing irrelevant variations. This facilitates automatic  
50 feature extraction, contrasting with "shallow" networks or conventional ML algorithms that rely on  
51 expert knowledge and engineering skills for designing feature extractors. This is a key rationale behind  
52 the increasing application of DL models over shallow networks in recent years (Frank et al., 2020).  
53 Structurally, the standard recurrent neural network (RNN), exemplified by long short-term memory

---

54 (LSTM), remains the foundational model architecture for DL-driven hydrological forecasting. As a  
55 subset of RNN in DL, LSTM has gained prominence for its efficacy in managing sequential data and  
56 capturing long-term dependencies. LSTM tackles the challenges of vanishing and exploding gradients in  
57 traditional RNNs when handling lengthy sequences through gated mechanisms, resulting in superior  
58 performance in time-dependent prediction tasks (Hochreiter and Schmidhuber, 1997).

59 DL has been extensively utilized in various fields. In hydrology, where processes are not yet fully  
60 understood, it exhibits promise in identifying physical processes through a data-mining lens. However,  
61 achieving accurate forecasting is not the sole aim. Hydrologists are interested in whether models are in  
62 line with fundamental physical principles, are interpretable, and contribute to scientific knowledge  
63 advancement. Traditional physics-based hydrological models generally provide better interpretability  
64 and physical consistency, relying less on data and complementing DL models. As a result, the fusion of  
65 physics-based mechanisms and data-driven models has garnered significant attention in recent years,  
66 showcasing potential in advancing scientific inquiry (Nearing et al., 2021; Shen, 2018). Currently, the  
67 coupling of DL and physics-based models focuses on four main aspects.

68 (1) Introducing physical mechanisms into DL models' loss functions

69 Worland et al. (2019) developed a multi-output multilayer perceptron (MLP) model to forecast flow  
70 duration curve (FDC) quantiles, incorporating FDC monotonicity constraints into the loss function. This  
71 approach resulted in forecasts that adhered to monotonicity and closely matched the FDC derived from  
72 observations. Wang et al. (2020) not only incorporated physical laws into the loss function but also  
73 integrated expert knowledge in the form of inequalities, constructing theory-guided neural networks  
74 (TGNN). TGNN demonstrated superior predictive performance compared to standard DL models. Xie  
75 et al. (2021) encoded three physical conditions in rainfall-runoff forecasting into the loss function.  
76 Experiments across 531 Catchment Attributes and Meteorology for Large-sample Studies (CAMELS)  
77 basins showed improvements in the average Nash-Sutcliffe efficiency (*NSE*) from 0.52 to 0.61, enhanced  
78 peak flow simulating, and reduced unreasonable negative values. Pokharel et al. (2023) tested the effects  
79 of incorporating mass balance, energy balance, and storage-discharge relationships into the loss function  
80 of DL models across 34 basins, finding performance improvements in some basins, particularly with  
81 mass and energy balance constraints, which were effective in 38% and 32% of basins, respectively. Frame

---

82 et al. (2023) concluded that strictly adhering to the principle of water balance may reduce forecasting  
83 accuracy due to data errors. However, DL models do not require the enforcement of the water balance  
84 principle and can adapt to data biases, and they perform better than the traditional hydrological models  
85 in flow forecasting.

86 (2) Using DL models as post-processors

87 Correcting errors in forecasting from physics-based models can significantly improve forecasting  
88 accuracy. Cho and Kim (2022) employed LSTM to learn correlations between meteorological data and  
89 WRF-Hydro forecast errors, applying this approach to calibrate WRF-Hydro forecasting. Experiments  
90 in South Korean basins showed *NSE* values reaching 0.95, compared to 0.72 before calibration. Similarly,  
91 Han and Morrison (2022) and Frame et al. (2021) applied LSTM to post-process multi-period forecasting  
92 from the National Water Model (NWM) in the United States. Boucher et al. (2020) utilized the simulated  
93 runoff of the GR4J hydrological model and observed water temperature as inputs to construct an MLP  
94 model, demonstrating notable improvements compared to models without assimilation. Cui et al. (2021)  
95 proposed a novel hybrid model combining the Xinanjiang (XAJ) hydrological model with LSTM for  
96 multi-step flood forecasting. This model used XAJ outputs as inputs to the LSTM, enhancing the physical  
97 mechanism of DL models. Yang et al. (2020) proposed a hybrid modeling framework that integrates a  
98 physically distributed hydrological model (GBHM), artificial neural networks (ANN), a categorization  
99 approach (CA), and computer vision (CV) to enhance hydrological simulations in data-scarce watersheds.  
100 They show that these models can significantly improve the ability to capture spatial variability and  
101 simulate extreme flow events. Li et al. (2014) proposed a black-box model which combines the back-  
102 propagation neural network (BPNN) with the K-nearest neighbor (KNN) algorithm, and developed two  
103 hybrid models (XBK and XSBK) by coupling the black-box routing module with the runoff generation  
104 and separation modules of the XAJ model. Applications in multiple watersheds demonstrate that these  
105 hybrid models outperform both the traditional BPNN and the XAJ model.

106 (3) Using DL models to calibrate parameters in traditional hydrological models

107 Tsai et al. (2021) proposed a parameter learning method to calibrate HBV model parameters. The  
108 DL model generated parameters instead of directly outputting runoff, which were then combined with  
109 inputs to produce runoff through the physical model. Applying this method across 1,802 basins showed

---

110 median Kling-Gupta Efficiency (*KGE*) values improving from 0.48 to 0.59 compared to calibration via  
111 evolutionary algorithms followed by parameter regionalization. Similarly, Feng et al. (2023, 2022), Shen  
112 et al. (2023) and Song et al. (2024) used DL models to calibrate HBV model parameters based on  
113 meteorological data and basin attributes, driving hydrological models to simulate runoff. In addition to  
114 the above calibration of lumped model parameters, a similar method is also used to calibrate the routing  
115 model parameters. Zhong et al. (2024a, 2024b) used DL model to calibrate parameters in the Muskingum-  
116 Cunge method and construct a distributed physics-driven DL hydrological model. Bindas et al. (2024)  
117 introduced a novel differentiable routing method ( $\delta$ MC-JuniatahydroDL2) combining the Muskingum-  
118 Cunge routing model with neural networks to infer Manning's roughness and channel geometry  
119 parameters. The method provided more accurate long-term routing forecasts, especially in untrained sub-  
120 basins.

#### 121 (4) Designing DL models based on physical mechanisms

122 Encoding rules directly into neural networks represents a direct fusion of physics-based and data-  
123 driven models. Hoedt et al. (2021) modified LSTM structures to enforce water balance over specific  
124 periods. Experiments across 531 CAMELS basins showed improved peak flow performance despite no  
125 overall improvement in *NSE*. Wang and Gupta (2024) explored the use of mass-conserving perceptron  
126 (MCP)-based directed graph architectures to develop minimal and interpretable hydrological model  
127 structures within a single catchment. They found that this framework significantly enhances flow  
128 simulation performance, particularly when augmented with input bypass and bi-directional groundwater  
129 exchange mechanisms. Jiang et al. (2020) modified RNN structures to incorporate state variables (e.g.,  
130 soil moisture) from EXP-HYDRO model as recurrent unit states, combining these with other neural  
131 network layers to construct a physics-guided RNN. Experiments in 671 CAMELS basins demonstrated  
132 median *NSE* improvements from 0.60 to 0.71, with reductions in peak flow bias and improved baseflow  
133 simulations. De la Fuente et al. (2024) proposed HydroLSTM, which models hydrological principles to  
134 enhance interpretability, achieving comparable performance to LSTM models while requiring fewer unit  
135 states. Similarly, Li et al. (2024) embedded EXP-HYDRO processes into RNN units, developing a  
136 process-driven DL model that enhanced process understanding of rainfall-runoff relationships.  
137 Experiments across 531 CAMELS basins demonstrated improvements over LSTM model. Similarly, He

---

138 et al. (2024) proposed a deep process learning (DPL) approach, which allows neural networks to infer  
139 underlying process mechanisms from observational data by embedding intuitive physical laws of  
140 geosystems directly into the DL architecture as structural priors. Wang et al. (2024) introduced a novel  
141 distributed hydrological modeling framework combining HydroPy model principles encoded into RNN  
142 units and DL models to calibrate physical parameters, improving runoff and water volume simulation  
143 performance

144 Currently, the current integration of DL models with physical mechanisms mainly involves loosely  
145 coupled approaches, such as modifying loss functions or calibrating parameters. Even the more advanced  
146 methods which embed physical mechanisms directly into neural network layers, they are relied on  
147 relatively simple or empirical physical models. To achieve real breakthroughs in hydrological forecasting,  
148 it is still necessary to systematically integrate more complex hydrological physical processes into neural  
149 network architectures, thereby ensuring both rigorous physical interpretability and superior forecasting  
150 performance under future scenarios.

151 The XAJ model proposed by Zhao (1992, 1993) has been widely used for hydrological simulation  
152 and flood forecasting in China. The flow routing of the XAJ model includes hillslope routing and channel  
153 network routing (Yao et al., 2009, 2014), which are represented by linear reservoirs and Nash unit  
154 hydrographs (Singh, 1977), respectively. Compared with other lumped hydrological models, the XAJ  
155 model performs very well in the humid and semi-humid regions, which helps to better highlight the  
156 distinctive aspects of this study. The core innovation of this study is the development of a novel XAJRNN  
157 layer that converts the XAJ model's sophisticated runoff generation and flow routing mechanisms into  
158 differential equation form and embeds them within a conventional RNN unit framework by explicitly  
159 defining its state variables and fluxes. An explainable deep learning (EDL) model combining the  
160 XAJRNN layer and LSTM layer is constructed and tested in the Lushui River and Qingjiang River basins  
161 to demonstrate the advantages of the EDL model in flood simulation. The findings may offer a promising  
162 new avenue for tightly integrating complex hydrological processes into DL models to improve flood  
163 forecasting accuracy.

164 The rest of this paper is organized as follows. The case study and materials are introduced in Section  
165 2. Section 3 presents the methodologies. Section 4 evaluates and analyses the simulated results. Section

---

166 5 discusses the strengths as well as the weaknesses of the proposed model. Conclusions and outlook are  
167 given in Section 6.

## 168 **2 Study area and data**

### 169 **2.1 Study basin**

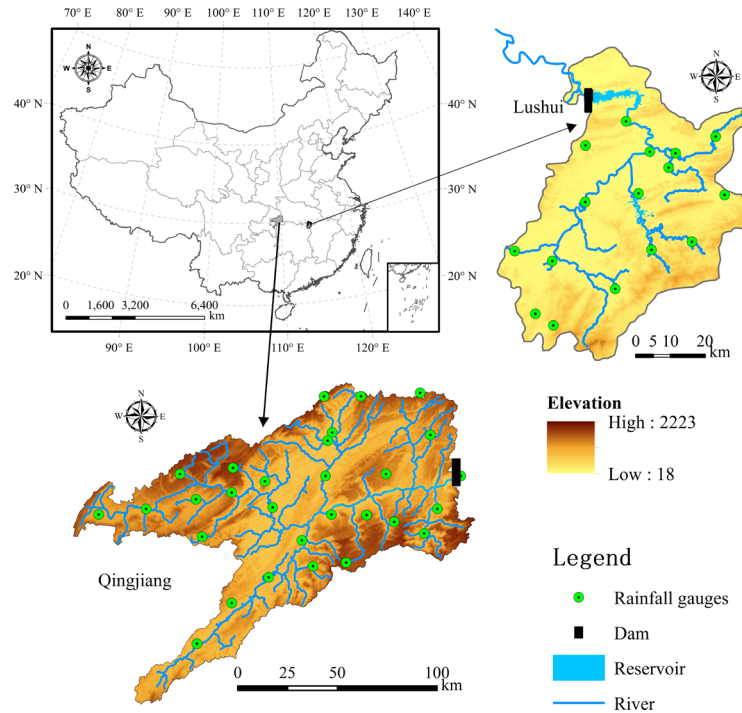
#### 170 **(1) Lushui River basin**

171 The Lushui River is a primary tributary of the middle Yangtze River, with a basin area of  
172 approximately 3,950 km<sup>2</sup>. The basin's terrain slopes from high elevations in the southeast to lower areas  
173 in the northwest. The basin is located in a subtropical monsoon climate zone, characterized by warm and  
174 humid conditions, with an average annual temperature of approximately 15.5°C and an average annual  
175 rainfall of 1,550 mm. The Lushui River's annual runoff volume reaches 3.03 billion m<sup>3</sup>, with rainfall  
176 concentrated from May to September, accounting for 70% of the annual total. At the river valley's outlet,  
177 the Lushui Reservoir has a total storage capacity of approximately 408 million m<sup>3</sup>, with only 163 million  
178 m<sup>3</sup> allocated for flood control. In early July 1995, the reservoir experienced its largest flood event, with  
179 an inflow peak of 4,500 m<sup>3</sup>/s and a three-day runoff of 500 million m<sup>3</sup>. In 2017, six flood events occurred,  
180 with peak inflows exceeding 1,000 m<sup>3</sup>/s, reaching a maximum inflow of 4,400 m<sup>3</sup>/s (Cui et al., 2021;  
181 Xiang et al., 2024). The geographical location of Lushui Reservoir is shown in Figure 1.

#### 182 **(2) Qingjiang River basin**

183 The Qingjiang River, a primary tributary of the Yangtze River in the middle reaches, has a basin  
184 area of approximately 17,000 km<sup>2</sup>. The region receives an average annual rainfall of 1,460 mm, with the  
185 majority falling between April and September, representing 75%–78% of the annual total. Situated in the  
186 heavy rainfall region of western Hubei Province, the basin's terrain facilitates the uplift of warm, moist  
187 air and is frequently affected by southwest cyclones. With a natural elevation drop of 1,430 m, the area  
188 features steep terrain and a high river gradient, leading to swift water flow convergence and significant  
189 fluctuations in flood levels. Consequently, the area is susceptible to severe rainfall and flood disasters.  
190 Along the main stream of the Qingjiang River, three sizable reservoirs exist, with the Shuibuya Reservoir  
191 serving as the central hub for the basin's cascade development, overseeing an area of roughly 10,860 km<sup>2</sup>.

192 Located in Badong County, Hubei Province, the Shuibuya Reservoir plays a crucial role in the  
 193 hydropower development of the Qingjiang River. The Qingjiang River basin experienced major floods  
 194 in 2016 and 2017, with peak inflow discharge of the Shuibuya Reservoir reached 13,100 m<sup>3</sup>/s and 6,710  
 195 m<sup>3</sup>/s, respectively. It greatly forms an integral component of the flood control system in the middle and  
 196 lower reaches of the Yangtze River (Zhou et al., 2014). This study specifically focuses on the basin  
 197 controlled by the Shuibuya Reservoir, as depicted in Figure 1.



198  
 199 **Figure 1: Sketch map of river networks and rainfall gauges in the Lushui River and Qingjiang River basins.**

200 **2.2 Data**

201 The study collected flood season data (Lushui River basin: May 1 to October 31, 2012–2019;  
 202 Qingjiang River basin: April 1 to October 31, 2012–2020) that includes rainfall, pan evaporation, and  
 203 inflow datasets. It should be noted that the time step of these data series is 3 h in the Lushui River basin,  
 204 whereas it is 6 h in the Qingjiang River basin. For Lushui River basin, 3 h rainfall data from 17 gauges,  
 205 3 h pan evaporation, and 3 h inflow discharge was collected. The data from 2012 to 2016 were used for  
 206 training, and the data from 2017 to 2019 for testing. For Qingjiang River basin, 6 h rainfall from 28  
 207 gauges, 6 h pan evaporation, and 6 h inflow discharge was gathered. The data from 2012 to 2016 were  
 208 used for training, and the data from 2017 to 2020 for testing. The Thiessen polygon method was used to



---

209 calculate the areal mean rainfall and pan evaporation for both basins.

## 210 **3 Methodologies**

### 211 **3.1 XAJRNN neural network layer**

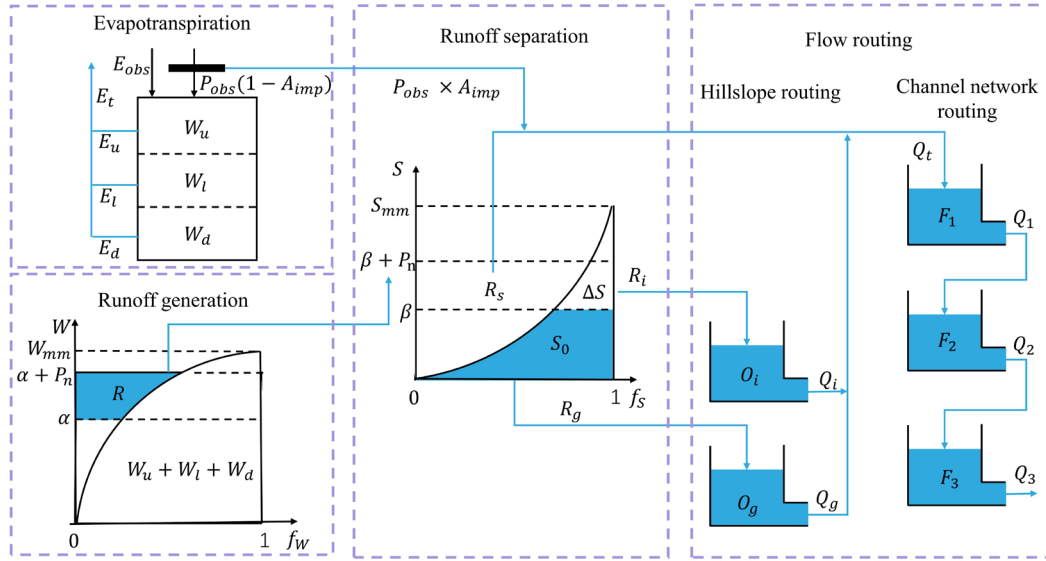
#### 212 **3.1.1 XAJ model overview**

213 Zhao (1992, 1993) firstly proposed the XAJ model for rainfall-runoff simulation and flood  
214 forecasting in the 1970s, and it is a classic conceptual hydrological model and has been widely used in  
215 China. The core concept of the XAJ model is the runoff formation on repletion of storage: runoff is not  
216 produced until the soil moisture content of the aeration zone reaches the field capacity. Once this  
217 threshold is exceeded, all additional rainfall is converted directly into runoff without further loss. Runoff  
218 production at a specific point occurs only after the tension water storage at that point is fully saturated.  
219 To represent the spatial heterogeneity of tension water capacity within a basin, the model introduces a  
220 tension water capacity curve. In terms of runoff separation, the model, based on empirical observations  
221 and theoretical studies, adds an additional component: interflow, on top of the original division into  
222 surface runoff and groundwater runoff (Yao et al., 2009, 2014). In this study, the evapotranspiration of  
223 the XAJ model uses a three-layer soil moisture model. The runoff generation uses a tension water  
224 capacity curve (Zhao, 1992, 1993). In the runoff separation, the runoff is divided into three types using  
225 the free water capacity curve: surface runoff, interflow runoff, and groundwater runoff. The flow routing  
226 includes both hillslope routing and channel network routing submodules, which use linear reservoirs and  
227 Nash unit hydrographs (Singh, 1977), respectively. The logical structure of the XAJ model is shown in  
228 Figure 2.

229 The model consists of input variables, state variables, fluxes, output variables, and parameters, along  
230 with their corresponding mathematical equations. Input variables include areal mean rainfall and  
231 measured pan evaporation, while the output variable is the simulated runoff. State variables represent  
232 physical quantities that characterize the basin's state, and their dimensions are independent of time (La  
233 Follette et al., 2021). The state variables of the XAJ model are shown in Table A1. Fluxes describe the  
234 exchange of water within the basin or between the basin and external environments. These can be

235 expressed as functions of state variables or other fluxes, and their dimensions are time-dependent (La  
 236 Follette et al., 2021). The fluxes of the XAJ model are shown in Table A2. The mathematical equations  
 237 can be divided into state variable control equations and constitutive equations for fluxes. The control  
 238 equations describe how state variables evolve over time, while the constitutive equations establish the  
 239 relationships between unknown fluxes and state variables or known fluxes. Detailed information on the  
 240 XAJ model is provided in Text A1.

241



242

243

**Figure 2: Structure diagram of the XAJ model.**

244

### 3.1.2 Derivation of XAJRNN

245

246

247

248

249

Establishing the XAJ model in the watershed can be considered a complete system that represents changes in state variables within the watershed, such as the variation in the average tension water storage of the upper soil layer. At the same time, the XAJ model also describes how the watershed system responds to specific input conditions. These responses can be expressed through a combination of ordinary differential equations (ODE) and output equations:

250

$$\begin{cases} \frac{d}{dt} h(t) = F(h(t), x(t); \varphi_f) \\ y(t) = G(h(t), x(t); \varphi_g) \end{cases} \quad (1)$$

251

252

253

where:  $h(t)$  represents the state variables of the XAJ model (as shown in Table 1).  $x(t)$  represents the input variables of the XAJ model ( $P_{obs}$  and  $E_{obs}$ ).  $y(t)$  represents the output flow of the XAJ model.  $\varphi_f$  and  $\varphi_g$  are parameters in the XAJ model (as shown in Table A3).  $F(\cdot)$  and  $G(\cdot)$  represent the

254 mathematical equations and functions in the model. The above equations form explicit continuous  
 255 equations, but in practice, implicit discrete equations are generally used to obtain numerical solutions:

$$256 \quad \begin{cases} h(t) = f(h(t-1), x(t); \varphi_f) \\ y(t) = g(h(t), x(t); \varphi_g) \end{cases} \quad (2)$$

257 Ordinary RNN is neural network structures specifically designed for handling sequential data, as  
 258 shown in Figure 3(a). RNN utilizes time-dependent relationships in sequences by storing previous state  
 259 information to assist in current computations (Rumelhart et al., 1986). At  $t$ th time step, the calculation  
 260 in an RNN unit can be divided into two steps: the first step is updating the hidden state ( $h_t$ ), and the  
 261 second step is calculating the output ( $y_t$ ). The calculation formulas are as follows:

$$262 \quad \begin{cases} h_t = \sigma(W_{xh} \cdot x_t + W_{hh} \cdot h_{t-1} + b_h) \\ y_t = \sigma(W_{hy} \cdot h_t + b_y) \end{cases} \quad (3)$$

263 where,  $h_t$ ,  $x_t$  and  $y_t$  are the state, input, and output at  $t$ th time, respectively.  $W_{xh}$ ,  $W_{hh}$  and  $W_{hy}$   
 264 are the weight parameters.  $b_h$  and  $b_y$  are bias parameters.  $\sigma$  is the nonlinear activation function.

265 It can be observed that Eq. (2) and (3) have a similar structure. Both equations consist of two parts:  
 266 an ordinary differential equation and an output equation, and they share a highly similar structure.  
 267 Specifically, in the ordinary differential equation part, both equations include the state variable from  
 268 the previous time step ( $h(t-1)$ ), the state variable at the current time step ( $h(t)$ ), the input ( $x$ ), and the  
 269 parameters ( $(\varphi, W, b)$ ). In the output equation part, both equations rely on the current state variable  
 270 ( $h(t)$ ), the output ( $y$ ), and the same set of parameters ( $(\varphi, W, b)$ ). Therefore, in this study, we modify  
 271 the ordinary RNN unit structure by replacing the original equations and parameters with those derived  
 272 from the XAJ model, resulting in the XAJRNN. Similar to the ordinary RNN structure (Rumelhart et al.,  
 273 1986), the backbone of the XAJRNN layer consists of recurrent units that provide memory of past  
 274 sequences. In the XAJRNN layer structure, the connections between the recurrent units are represented  
 275 by implicit discrete equations (Eq. 3), and the parameters (i.e., weight parameters and bias parameters)  
 276 in the ordinary RNN unit are replaced by the physically meaningful parameters (as depict in Table A3)  
 277 from the XAJ model. Niu et al. (2019) demonstrated the connection between RNN network architecture  
 278 and numerical methods for ODE, theoretically supporting the use of XAJRNN for solving the dynamics  
 279 of the XAJ model system. Table A4 summarizes the pseudocode for implementing the XAJRNN unit.

280 The internal computation process of the XAJRNN unit is explained below using pseudocode and

---

281 equations provided in the appendix. For each XAJRNN unit, it is first necessary to initialize the  
282 watershed state, including the areal mean tension water storage of the upper ( $W_u$ ), lower ( $W_l$ ), and deep  
283 ( $W_d$ ) soil layers of the watershed, the areal mean free water storage ( $S_0$ ), the storage of the interflow  
284 linear reservoir ( $O_i$ ), the storage of the groundwater linear reservoir ( $O_g$ ), and the storage of the three  
285 reservoirs in the Nash unit hydrograph ( $F_1$ ,  $F_2$  and  $F_3$ ). Then, the hydrological response of the  
286 XAJRNN unit at each time step is carried out through a "step\_function", in which all computations are  
287 encapsulated. The network calls the "step\_function" in a sequential manner. The function mainly includes  
288 the following four sub-functions:

289 (1) Based on the three-layer soil moisture model and the tension water capacity curve, the runoff  
290 generation from the permeable portion of the watershed is calculated. The corresponding equations are  
291 A1 to A12, and the main parameters involved include  $A_{imp}$ ,  $K_c$ ,  $c$ ,  $b$ ,  $W_{um}$ ,  $W_{lm}$ , and  $W_{dm}$ . Then,  
292 the areal mean tension water storage of the upper ( $W_u$ ), lower ( $W_l$ ), and deep ( $W_d$ ) soil layers of the  
293 watershed is updated, which will serve as the initial values for the next period. This corresponds to  
294 equations A13 to A20. The main outputs obtained in this sub-function are the runoff ( $R$ ), actual  
295 evapotranspiration ( $E_t$ ), and net rainfall ( $P_n$ ).

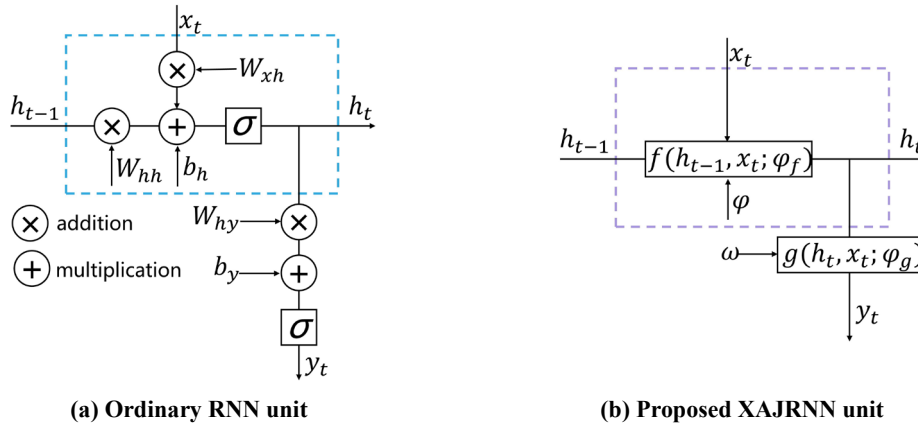
296 (2) The runoff ( $R$ ) is divided into different components using the free water capacity curve. The  
297 corresponding equations are A21 to A25, and the parameters involved include  $S_m$ ,  $ex$ ,  $K_i$ , and  $K_g$ .  
298 Then, the areal mean free water storage ( $S_0$ ) is updated according to equation A26. The outputs obtained  
299 in this sub-function are surface runoff ( $R_s$ ), interflow runoff ( $R_i$ ), and groundwater runoff ( $R_g$ ).

300 (3) The interflow runoff ( $R_i$ ) and groundwater runoff ( $R_g$ ) obtained earlier are routed over the  
301 hillslope using the linear reservoir method. The corresponding equations are A27 and A28, with  
302 parameters  $c_i$  and  $c_g$ . Then, combined with the surface runoff ( $R_s$ ), the total inflow ( $Q_t$ ) into the  
303 channel network is calculated, corresponding to equation A29. The outputs obtained are the outflow of  
304 the interflow linear reservoir ( $Q_i$ ), the outflow of the groundwater linear reservoir ( $Q_g$ ), and total inflow  
305 ( $Q_t$ ).

306 (4) The Nash unit hydrograph method is used to perform channel network routing, resulting in the  
307 final outflow ( $Q$ ). The corresponding equations are A30 to A33, and the parameter involved is  $K_f$ . All  
308 of the above physical parameters are automatically adjusted during the model training process through

309 gradient descent and backpropagation.

310



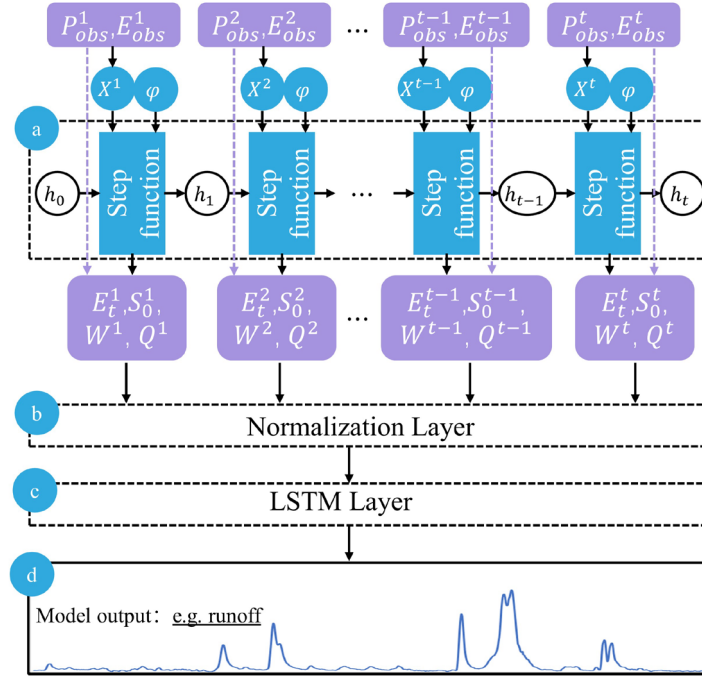
311 **Figure 3: The structures of ordinary RNN unit and proposed XAJRNN unit.**

## 312 3.2 Model setup

### 313 3.2.1 EDL model

314 The proposed EDL model consists of the inputs, three neural network layers, and the outputs. First,  
315 the XAJRNN layer, as discussed in Section 3.1.2, processes the input data to generate outputs. This neural  
316 network layer follows the water balance principle and uses the physical sub-processes of the XAJ model  
317 to describe the runoff generation and routing process. The output variables, significantly influenced by  
318 the runoff process, are then passed to the Normalization layer. The purpose of this layer is to normalize  
319 the data, helping the EDL model converge faster during training, increasing training stability, and  
320 reducing the impact of differences between features. Specifically, the normalization layer adjusts the data  
321 so that the mean is 0 and the standard deviation is 1. The normalized data is then passed into the LSTM  
322 neural network layer for training. The choice of LSTM layers is based on two primary considerations:  
323 first, its memory cells can retain hydrological information over extended periods, effectively capturing  
324 the temporal dependencies of the rainfall–runoff process to enhance flood simulating accuracy; and  
325 second, many studies have demonstrated that LSTM consistently improves hydrological model  
326 simulation performance. For example, Alizadeh et al. (2021) demonstrated the SAINA-LSTM model  
327 outperforms the EnsPost and MS-EnsPost in low, medium, and high flow ranges, as well as in 1 to 7 day  
328 forecast horizons, and significantly reduces the root mean square error of flow predictions. Additionally,

329 Xu et al. (2022) combined the particle swarm optimization (PSO) algorithm with the LSTM model to  
 330 obtain the PSO-LSTM model. The research results show that the PSO-LSTM model outperforms the  
 331 Artificial Neural Network (ANN) and PSO-ANN at all stations in the basin. Finally, the trained EDL  
 332 model outputs the simulated runoff.  
 333



334  
 335 **Figure 4: The structure of the proposed EDL model. (a) The structure network schematic graph of the**  
 336 **XAJRNN layer.  $h$  represents the state variables in the XAJRNN layer (as shown in Table A1).  $\varphi$  represents**  
 337 **the parameters in the XAJRNN layer (as shown in Table A3). (b), (c), and (d) represent the normalization**  
 338 **layer, LSTM layer, and output results, respectively.**

339 For the EDL model, similar to the traditional XAJ model, the XAJRNN layer takes areal mean  
 340 rainfall ( $P_{obs}$ ) and pan evaporation ( $E_{obs}$ ) as input data, with a shape of [batch size, sequence length, 2  
 341 (input feature dimensions)]. The output physical quantities of interest are the actual evapotranspiration  
 342 ( $E_t$ ), the areal mean free water storage ( $S_0$ ), the areal mean tension water storage ( $W$ ), and outflow  
 343 discharge of the basin ( $Q$ ). The selection of these four variables as the output of the XAJRNN layer is  
 344 primarily based on their high hydrological relevance to flood forecasting. Actual evapotranspiration ( $E_t$ )  
 345 is a key component of the hydrological cycle, directly affecting water availability and playing a crucial  
 346 role in runoff processes and flood simulation. Areal mean free water storage ( $S_0$ ) and tension water  
 347 storage ( $W$ ) represent the states of free water and water under tension in the watershed, reflecting the

---

348 basin storage capacity, which in turn influences flood occurrence and intensity. Outflow discharge ( $Q$ ),  
349 as the direct output of the basin system, is a core indicator for flood simulation. The selection of these  
350 variables fully considers their physical significance and practical application value in flood simulation.  
351 These four physical quantities, along with the two input sequences, form a new sequence that serves as  
352 input for subsequent layers. The shape of the new input is [batch size, sequence length, 6 (new input  
353 feature dimensions)]. After passing through normalization layers and LSTM layers, the final simulated  
354 flow sequence is obtained. Following the general optimization methods of DL models, the parameters of  
355 the XAJRANN and LSTM layer in the EDL model are optimized using gradient descent, specifically  
356 with the *Adam* optimizer, to minimize the loss function. In our study, a separate model was trained for  
357 each basin for flood simulation and forecasting, whose parameters were directly updated using the  
358 standard end-to-end backpropagation approach. The model is trained with *NSE* as the loss function and  
359 a learning rate of 0.001. The maximum number of iterations is set to 200, and training samples are reused  
360 in each training cycle until convergence is achieved (i.e., the absolute difference in *NSE* between  
361 consecutive cycles is less than 0.001).

### 362 **3.2.1 Benchmark model**

363 To compare the performance of the EDL model, three benchmark models are established. The first  
364 benchmark model is the ordinary XAJ model, which also takes areal mean rainfall and evaporation as  
365 input to illustrate the role of the XAJRNN layer in the EDL model. The input is the observed areal mean  
366 rainfall ( $P_{obs}$ ) and pan evaporation ( $E_{obs}$ ), the output is the simulated flow discharge. Unlike the previous  
367 DL model, we use the genetic algorithm (GA) to calibrate model parameters. The GA searches in a  
368 population of points, uses the encoding of parameter sets, and uses probabilistic transition rules. There  
369 are four GA hyperparameters: crossover probability parameter ( $p_c$ ), mutation probability parameter ( $p_m$ ),  
370 population size parameter ( $p_{size}$ ) and the maximum number of generation ( $T_{max}$ ). Referring to the research  
371 results of Cheng et al. (2006), the above hyperparameters are set to,  $p_c=0.8$ ,  $p_m=0.1$ ,  $p_{size}=150$ , and  
372  $T_{max}=1500$ . The second benchmark model is LSTM model, which differs from the EDL model only in  
373 the absence of the XAJRNN layer; the rest of the architecture, including the normalization layer and  
374 LSTM layer, remains the same. The purpose of LSTM model is to compare the contribution of XAJRNN

375 layer to the simulation performance in the EDL model. In order to reduce the impact of the training  
 376 process on the model performance, the training process and hyperparameters of the LSTM model are the  
 377 same as those of the EDL model.

378 **Table 1: Optimal parameters of the ordinary XAJ model calibrated using the GA algorithm.**

Parameter	Value range	Lushui River basin	Qingjiang River basin
$K_c$	[0.6,1.5]	0.95	0.85
$c$	[0.01,0.2]	0.18	0.19
$W_{um}$	[5,30]	28.75	23.15
$W_{lm}$	[60,90]	84.36	64.47
$W_{dm}$	[15,60]	23.19	15.60
$A_{imp}$	[0.01,0.2]	0.02	0.01
$b$	[0.1,0.4]	0.40	0.35
$S_m$	[10,50]	49.97	39.86
$ex$	[1,1.5]	1.08	1.06
$K_i$	[0.1,0.55]	0.19	0.37
$K_g$	[0.7- $K_i$ ]	0.51	0.33
$c_i$	[0.1,0.9]	0.87	0.89
$c_g$	[0.9,0.988]	0.98	0.97
$K_f$	[0.1,10]	3.99	1.58

379  
 380 The third benchmark model is the XAJ-LSTM hybrid model, which utilizes the simulated discharge  
 381 generated by the ordinary XAJ model as its primary input, augmented by observed areal mean rainfall  
 382 and pan evaporation data. The final output of XAJ-LSTM hybrid is the simulated flow discharge.  
 383 Similarly, the training process and hyperparameter configurations for the XAJ-LSTM model are kept  
 384 consistent with those used in the two previous benchmark models. The purpose of this benchmark model  
 385 is to demonstrate the superior performance of the proposed EDL model in comparison to using the LSTM  
 386 layers solely for hydrological post-processing.

### 387 3.3 Evaluation metrics

388 The overall performance of the models is evaluated using *NSE* (Nash and Sutcliffe, 1970), relative  
 389 error (*RE*), and root mean squared error (*RMSE*). The calculation formulas are as follows:

$$390 \quad NSE = 1 - \frac{\sum_{i=1}^N (Q_{o,i} - Q_{f,i})^2}{\sum_{i=1}^N (Q_{o,i} - \bar{Q}_o)^2} \quad (4)$$



---

391 
$$RE = \frac{\sum_{i=1}^N Q_{f,i} - \sum_{i=1}^N Q_{o,i}}{\sum_{i=1}^N Q_{o,i}} \times 100\% \quad (5)$$

392 
$$RMSE = \sqrt{\frac{\sum_{i=1}^N (Q_{f,i} - Q_{o,i})^2}{N}} \quad (6)$$

393 where  $N$  is the number of samples,  $Q_o$ ,  $\bar{Q}_o$  and  $Q_{f,i}$  represent the observed inflows, mean value,  
 394 and simulated inflows, respectively.

395 To further evaluate the performance of the four models for flood event simulation, the flood peak  
 396 relative error ( $PRE$ ) and the flood peak timing difference ( $\Delta T$ ) are calculated by the following formulas:

397 
$$PRE = \frac{Q_{f,peak} - Q_{o,peak}}{Q_{o,peak}} \times 100\% \quad (7)$$

398 
$$\Delta T = T_o - T_f \quad (8)$$

399 where  $Q_{o,peak}$  and  $Q_{f,peak}$  represent the observed and simulated peak inflow discharge.  $T_o$  and  $T_f$   
 400 are the observed and simulated times of peak discharges occurred. If  $\Delta T$  is positive, the simulated peak  
 401 discharge occurs early than the observed peak discharge; and vice versa.

## 402 **4 Results**

### 403 **4.1 Comparison of model performance**

404 Table 2 presents the evaluation metrics for flood simulation using four models (EDL, XAJ, LSTM,  
 405 and XAJ-LSTM) in the Lushui River and Qingjiang River basins. The evaluation metrics include  $NSE$ ,  
 406  $RE$ , and  $RMSE$  values for both training and test phases. In the Lushui River basin, the EDL model  
 407 demonstrated outstanding performance in both training and test periods. For the whole flow data series,  
 408 EDL achieved an  $NSE$  of 0.98 during the test period, with the lowest  $RMSE$  (43.71 m<sup>3</sup>/s) and a small  
 409 relative error ( $RE = -2.69\%$ ). These results outperformed both XAJ ( $NSE = 0.90$ ,  $RMSE = 89.60$  m<sup>3</sup>/s),  
 410 LSTM ( $NSE = 0.96$ ,  $RMSE = 54.27$  m<sup>3</sup>/s), and XAJ-LSTM ( $NSE = 0.92$ ,  $RMSE = 73.54$  m<sup>3</sup>/s). A similar  
 411 trend was observed in the Qingjiang River basin. the EDL model achieved an  $NSE$  of 0.92 and  $RMSE$  of  
 412 167.94 m<sup>3</sup>/s, maintaining a lower error compared to XAJ ( $RMSE = 231.17$  m<sup>3</sup>/s), LSTM ( $RMSE = 155.71$   
 413 m<sup>3</sup>/s), and XAJ-LSTM ( $RMSE = 227.62$  m<sup>3</sup>/s). These results indicate that the EDL model generalizes  
 414 well to different hydrological conditions.

415 Furthermore, as noted in Section 3.1.2, the XAJRNN layer within the EDL model can directly output

416 simulated outflow (Q). To evaluate its performance, we extracted the runoff from the XAJRNN layer and  
 417 compared it against observed streamflow in these two basins. The results are described as follows: in the  
 418 Lushui River basin, the training period yielded  $NSE=0.92$ ,  $RE=4.02\%$ ,  $RMSE=74.69$  m<sup>3</sup>/s, while the  
 419 testing period yielded  $NSE=0.90$ ,  $RE=10.87\%$ ,  $RMSE=86.98$  m<sup>3</sup>/s. In the Qingjiang River basin, the  
 420 training period achieved  $NSE=0.89$ ,  $RE=3.84\%$ ,  $RMSE=172.64$  m<sup>3</sup>/s, and the testing period  $NSE=0.86$ ,  
 421  $RE=-7.17\%$ ,  $RMSE=198.74$  m<sup>3</sup>/s. Compared with the XAJ model, the runoff simulated by the XAJRNN  
 422 layer shows overall improvement. However, its accuracy still falls short of the full EDL model. These  
 423 findings confirm that while the XAJRNN layer has advantages over the standard XAJ model, integrating  
 424 it with the LSTM layer could improve simulation accuracy.

425 It is important to note that the  $RMSE$  values of the two basins in Table 2 differ significantly.  
 426 Specifically, the  $RMSE$  in the Lushui River basin is noticeably lower than that in the Qingjiang River  
 427 basin. A possible reason for this difference is that, based on statistical calculations, the annual average  
 428 flow of the Qingjiang River basin is 290 m<sup>3</sup>/s, whereas that of the Lushui River basin is only 96 m<sup>3</sup>/s.  
 429 Additionally, the overall simulation performance in the Lushui River basin is better than in the Qingjiang  
 430 River basin. During the test phase, the LSTM model demonstrated better simulation performance in the  
 431 Qingjiang River basin, primarily due to the close integration of our EDL model with the XAJ model.  
 432 Specifically, the XAJRNN layer in the EDL model adopts the runoff generation and routing principles  
 433 of the XAJ model, and the model performance is closely related to the simulation accuracy of the XAJ  
 434 model. When the XAJ model performs well, the EDL model also achieves better  $NSE$ ,  $RE$ , and  $RMSE$   
 435 for the Qingjiang River.

436 **Table 2: Comparative analysis of model simulation accuracy evaluation metrics.**

Basin	Model	Training period			Test period		
		$NSE$	$RE$ (%)	$RMSE$ (m <sup>3</sup> /s)	$NSE$	$RE$ (%)	$RMSE$ (m <sup>3</sup> /s)
Lushui River	EDL	0.98	1.59	34.11	0.98	-2.69	43.71
	XAJ	0.86	-26.07	93.83	0.90	-18.50	89.60
	LSTM	0.97	-1.90	44.87	0.96	-0.61	54.27
	XAJ-LSTM	0.93	4.24	70.90	0.92	19.06	73.54
Qingjiang River	EDL	0.95	1.10	104.09	0.92	-8.74	167.94
	XAJ	0.85	5.91	182.05	0.85	-7.92	231.17
	LSTM	0.90	-4.16	147.89	0.93	-6.19	155.71
	XAJ-LSTM	0.88	1.56	164.52	0.86	-11.80	227.62

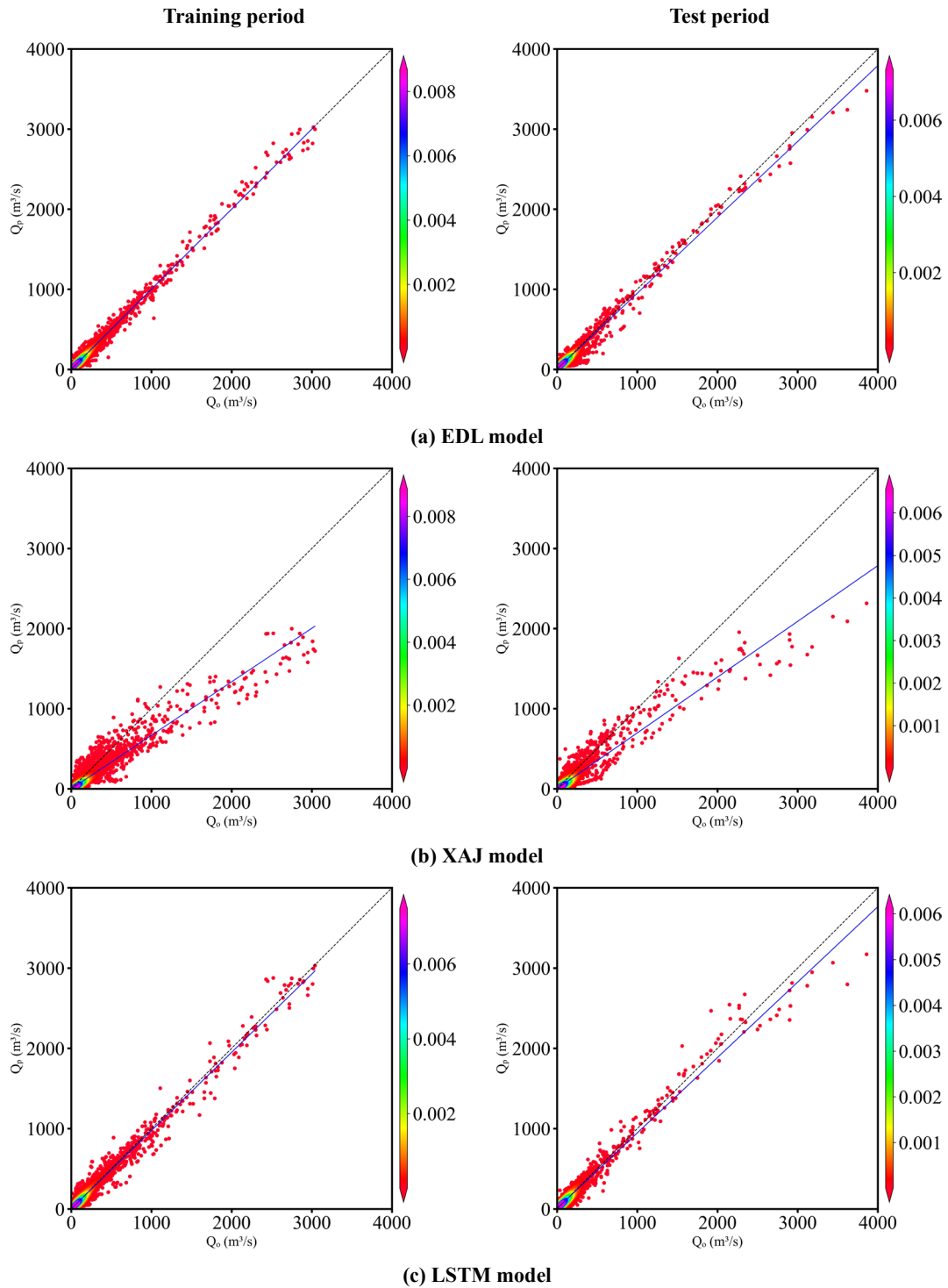
---

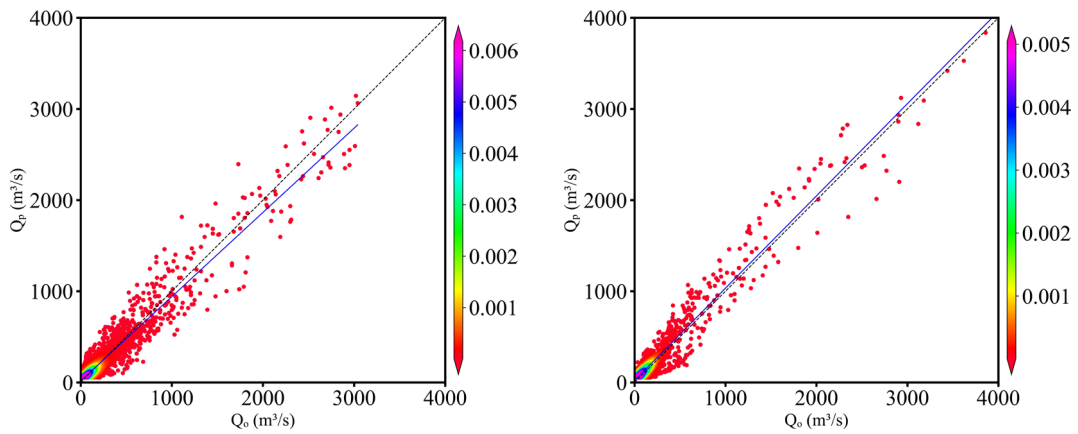
437

438 Figure 5 and Figure 6 respectively present the scatter plots of flood simulation results for the Lushui  
439 River and Qingjiang River basins using the EDL model, the XAJ model, the LSTM model, and XAJ-  
440 LSTM model. In Figure 5(a), during the training period, the scatter points of the EDL model are tightly  
441 clustered and evenly distributed around the 1:1 ideal line. However, during the test period, in the range  
442 where observed flow exceeds 3,000 m<sup>3</sup>/s, most scatter points are located below the 1:1 ideal line. As  
443 shown in Figure 5(b), the scatter points of the XAJ model are generally more dispersed compared to the  
444 EDL model, and fall noticeably below the 1:1 ideal line across both the training and test periods. In  
445 Figure 5(c), the scatter points of the LSTM model during the training period are evenly distributed around  
446 the 1:1 ideal line but are more dispersed than those of the EDL model. In Figure 5(d), the scatter points  
447 of the XAJ-LSTM model exhibit a distribution that lies between those of the XAJ and LSTM models,  
448 with a higher degree of dispersion compared to the tightly grouped points of the EDL model. During the  
449 test period, the scatter points in the low to medium flow range are evenly distributed around the 1:1 ideal  
450 line, similar to the EDL model, but in the range where the observed flow exceeds 3,000 m<sup>3</sup>/s, most scatter  
451 points are below the 1:1 ideal line. The reason that the scatter points fall below the 1:1 ideal line in the  
452 range where the observed flow exceeds 3,000 m<sup>3</sup>/s may be due to the fact that during the training period,  
453 there were few flow values exceeding 3,000 m<sup>3</sup>/s, while in the test period, there were relatively more  
454 high flows exceeding 3,000 m<sup>3</sup>/s. In summary, it can be concluded that the scatter plots of the EDL model  
455 are relatively better, while the scatter plots of the XAJ and LSTM models are relatively worse.

456 In Figure 6 (a), the scatter points of the EDL model are very compact and evenly distributed on both  
457 sides of the 1:1 ideal line during the training period. However, the scatter points are more loosely  
458 distributed, and some scatter points are obviously below the 1:1 ideal line during the test period. As  
459 shown in Figure 6 (b), the scatter points of the XAJ model during the training period are more scattered  
460 than the EDL model, and the scatter points are obviously deviated from the 1:1 ideal line in the range  
461 where observed flow exceeds 4,000 m<sup>3</sup>/s. During the test period, the scatter point distribution of the XAJ  
462 model is looser, and the scatter points are farther from the 1:1 ideal line in the range where the observed  
463 flow exceeds 4,000 m<sup>3</sup>/s. As shown in Figure 6 (c), the scatter point distribution of the LSTM model  
464 during the training period is similar to that of the EDL model. During the test period, it is also similar to

465 the EDL model, but the scatter points are obviously below the 1:1 ideal line in the range where the  
466 observed flow exceeds 6,000 m<sup>3</sup>/s. In Figure 6(d), the scatter points of the XAJ-LSTM model are more  
467 dispersed around the 1:1 ideal line than those of the EDL model. In summary, it can be concluded that  
468 the scatter plots of the EDL model are relatively better than these of the XAJ and LSTM models.

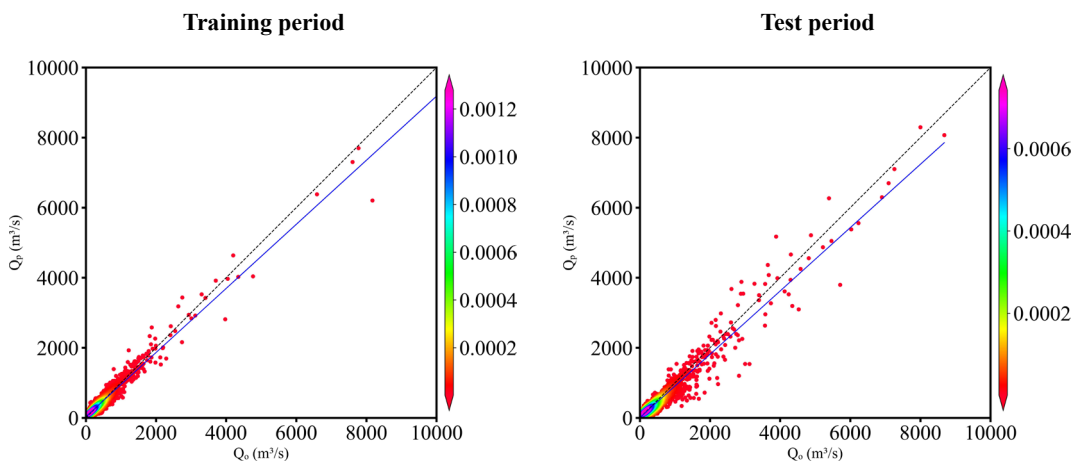




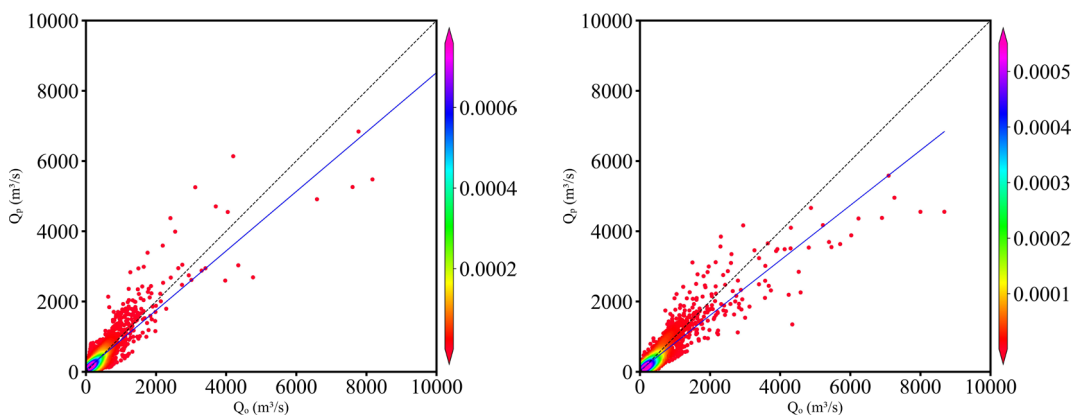
(d) XAJ-LSTM model

469 **Figure 5: Scatter plots of observed ( $Q_o$ ) and simulated ( $Q_p$ ) flow discharges by four models in the Lushui River**  
 470 **basin. The color bar represents the density of the scatter distribution. The denser the scatter distribution, the**  
 471 **higher the corresponding density value in color.**

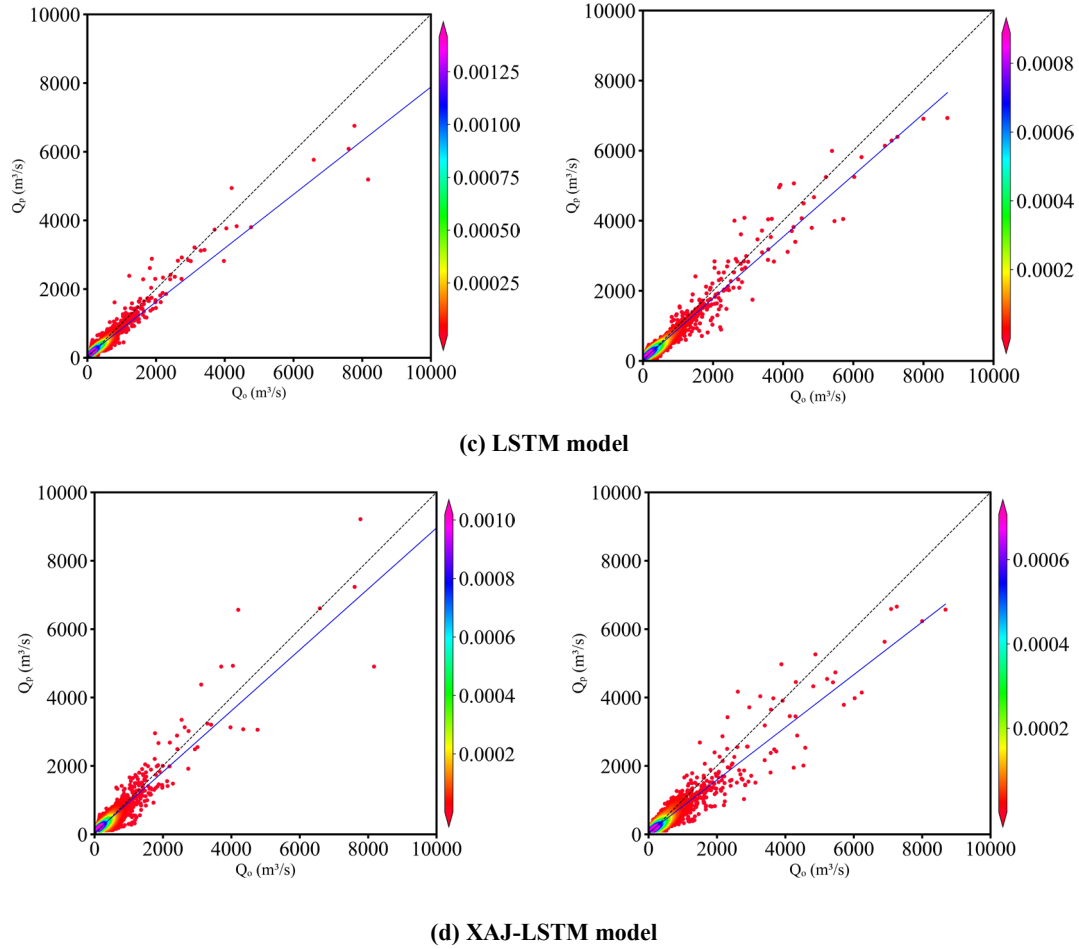
472



(a) EDL model



(b) XAJ model



473 **Figure 6: Scatter plots of observed ( $Q_o$ ) and simulated ( $Q_p$ ) flow discharge by four models in the Qingjiang**  
 474 **River basin. The color bar represents the density of the scatter distribution. The denser the scatter**  
 475 **distribution, the higher the corresponding density value in color.**

#### 476 **4.2 Comparison of the effectiveness of flood events simulation**

477 Four major flood processes during the test period were selected in the Lushui River and Qingjiang  
 478 River basins as case study. The simulation evaluation metrics of the three models (EDL, XAJ, LSTM,  
 479 and XAJ-LSTM) in these four flood processes are shown in Tables 3 and 4, respectively. These evaluation  
 480 metrics include  $NSE$ ,  $RE$ ,  $RMSE$ ,  $PRE$ , and  $\Delta T$ . It should be specifically noted that if  $\Delta T$  is positive,  
 481 the simulated peak discharge occurs earlier than the observed peak discharge; and vice versa.

482 As shown in Table 3, the EDL model performed exceptionally well with high simulation accuracy,  
 483 the  $NSE$  ranged from 0.97 to 0.99,  $RE$  ranged from -7.54% to -1.9%, and  $RMSE$  was as low as 71.66  
 484  $m^3/s$ . Additionally, the EDL model's  $PRE$  was consistently below -12%, and  $\Delta T$  remained at 0,  
 485 highlighting its high reliability in simulating peak flow magnitude and timing. In contrast, the XAJ

486 model's *NSE* ranged from 0.65 to 0.93, with significant *RE* deviations and *RMSE* values much higher  
 487 than those of the EDL model, resulting in subpar overall performance. The LSTM model's *NSE* ranged  
 488 from 0.91 to 0.97, close to that of the EDL model, but its *RE* and *RMSE* were slightly less favorable,  
 489 resulting in marginally lower simulation accuracy. The XAJ-LSTM model achieves a slightly lower *NSE*  
 490 value compared to the EDL model, along with considerably higher *RE* and *RMSE*, indicating an overall  
 491 inferior predictive performance.

492 As shown in Table 4, the EDL model continued to demonstrate superior performance, with *NSE*  
 493 exceeding 0.95 in all cases except for extreme events, *RE* ranging from -4.7% to -0.17% with minimal  
 494 bias, and *RMSE* as low as 266.62 m<sup>3</sup>/s. Although the EDL model's performance slightly declined during  
 495 extreme events (e.g., 20200726), it still outperformed other models overall. The XAJ model's  
 496 performance in the Qingjiang River basin was significantly inferior to the EDL model, with *NSE* varying  
 497 widely, reaching as low as 0.32, *RE* deviations as high as 26.42%, and *RMSE* peaking at 1277.61 m<sup>3</sup>/s,  
 498 indicating its poor adaptability to complex events. The LSTM model's *NSE* ranged from 0.64 to 0.94,  
 499 overall better than the XAJ model, but its accuracy and timeliness in peak flow simulation were  
 500 insufficient during extreme events. For the 20200628-flood event, the performance of the XAJ-LSTM  
 501 model was comparable to that of the EDL model. While for the other three flood events, the EDL-based  
 502 approach performed much better than the XAJ-LSTM model.

503 **Table 3: Flood simulation evaluation metrics for different events in the Lushui River basin.**

Flood event	Model	<i>NSE</i>	<i>RE</i> (%)	<i>RMSE</i> (m <sup>3</sup> /s)	<i>PRE</i> (%)	$\Delta T$ (h)
20170624	EDL	0.98	-7.54	211.98	-11.99	0
	XAJ	0.83	-19.31	561.31	-26.62	0
	LSTM	0.91	-12.29	421.53	-21.7	-3
	XAJ-LSTM	0.91	-6.79	417.77	-20.84	-3
20170702	EDL	0.97	-3.53	138.01	-11.57	0
	XAJ	0.65	-24.8	468.94	-37.34	30
	LSTM	0.93	0.76	204.43	-12.59	27
	XAJ-LSTM	0.83	-6.28	325.57	-18.16	30
20170813	EDL	0.99	-1.9	71.66	-0.9	0
	XAJ	0.85	-18.28	351.25	-26.61	3
	LSTM	0.97	0.28	142.23	-7.31	0
	XAJ-LSTM	0.92	2.67	255.68	-1.86	3
20190526	EDL	0.98	-3.85	85.92	-0.78	0
	XAJ	0.93	1.23	175.86	-10.15	0
	LSTM	0.97	-4.49	109.74	0.45	0
	XAJ-LSTM	0.97	-0.76	113.95	-5.66	0

504

**Table 4: Flood simulation evaluation metrics for different events in the Qingjiang River basin.**

Flood event	Model	<i>NSE</i>	<i>RE</i> (%)	<i>RMSE</i> (m <sup>3</sup> /s)	<i>PRE</i> (%)	$\Delta T$ (h)
20171003	EDL	0.95	-4.43	244.26	-7.64	0
	XAJ	0.89	5.38	357.55	-8.59	0
	LSTM	0.85	-15.82	417.92	-27.02	0
	XAJ-LSTM	0.87	-9.36	382.81	-13.37	0
20200628	EDL	0.98	-0.17	266.62	-2.2	0
	XAJ	0.95	5.48	467.13	-7.34	0
	LSTM	0.94	-3.58	506.72	-11.95	0
20200717	XAJ-LSTM	0.97	-2.80	377.35	-8.29	0
	EDL	0.95	-1.74	533.14	-4.48	6
	XAJ	0.66	-23.15	1368.23	-28.61	0
	LSTM	0.91	-5.43	696.92	-20.18	0
20200726	XAJ-LSTM	0.78	-19.29	1100.59	-24.34	0
	EDL	0.61	-4.7	966.73	-9.45	-6
	XAJ	0.32	26.42	1277.61	-12.75	-6
	LSTM	0.64	1.84	931.87	-13.29	-6
	XAJ-LSTM	0.51	8.13	1089.91	-12.94	-6

505

506 In summary, the EDL model exhibited the best overall performance in flood simulations for both  
507 the Lushui and Qingjiang River basins, with high accuracy, low bias, and excellent stability, particularly  
508 in regular flood events. Although the performance of LSTM and XAJ-LSTM models were close to that  
509 of the EDL model overall, it was slightly lacking in extreme events. In comparison, the XAJ model  
510 lagged significantly in both accuracy and adaptability, making it less suitable for precise flood simulation.

511 The outstanding performance of the EDL model highlights its immense potential in flood simulation,  
512 especially in complex basin conditions and extreme flood events. This further proves the advancement  
513 and feasibility of the model obtained by coupling DL technology with traditional hydrological models in  
514 the field of hydrological simulation, and provides strong tool support for solving flood forecasting  
515 problems.

516 To visually demonstrate the advantages of the EDL model, Figure 7 and 8 respectively present the  
517 hydrographs of four flood events in the Lushui River and Qingjiang River basins, comparing the  
518 simulation results of the EDL model, XAJ model, LSTM model, and XAJ-LSTM model.

519 From Figure 7, it can be observed that the 20170624-flood event, all four models underestimated  
520 the peak flow discharge to varying degrees, but the EDL model performed relatively better and more  
521 accurately simulated the timing of the peak flow. In the 20170702 and 20170813 compound flood events,



---

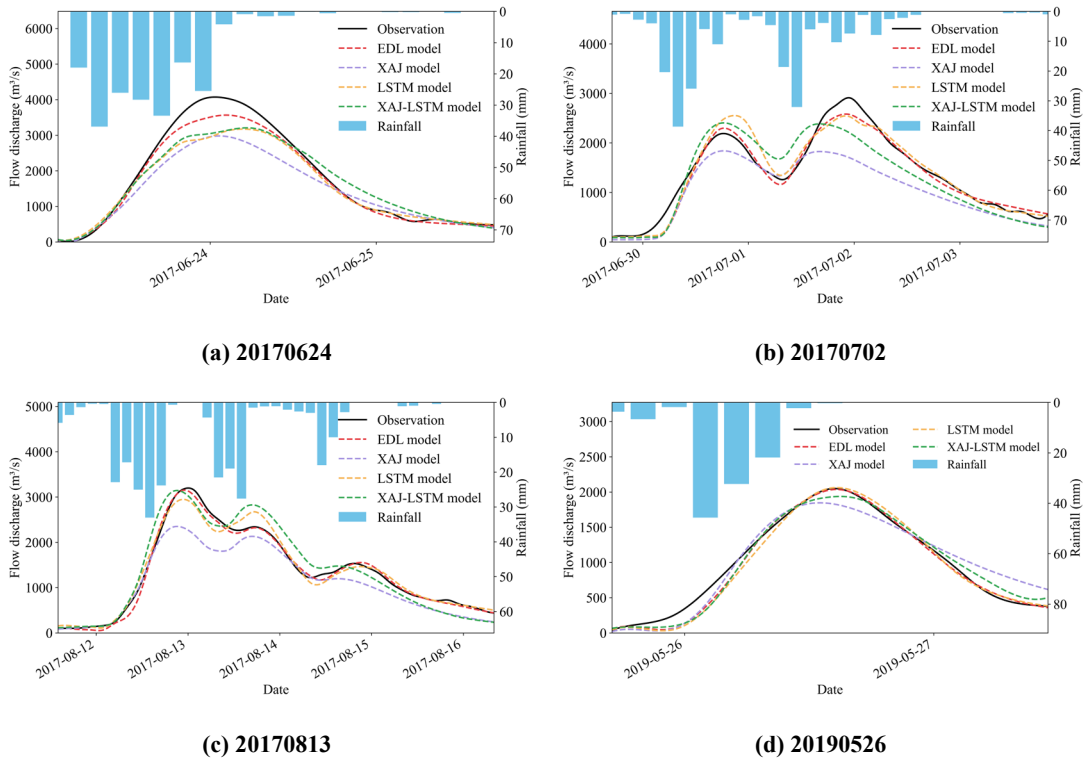
522 the EDL model's simulated hydrograph during the peak flow was closer to the observed hydrograph  
523 compared to the three benchmark models. For 20190526-flood event, both the EDL model and the LSTM  
524 model simulated the peak flow discharge well. However, in the 20170702 and 20190526 flood events,  
525 all four models exhibited delays, as evidenced by discrepancies in the rising speed during the flood rising  
526 phase compared to the observations. This may be due to the slow response of the model to rainfall.  
527 Overall, the EDL model performed well in simulating the hydrographs of the Lushui River basin,  
528 accurately capturing both the peak flow discharge and the timing of the peak.

529 Compared to the Lushui River basin, the simulation results of the four models in the Qingjiang  
530 River basin showed certain limitations, which were particularly evident in the 20200726-flood event as  
531 shown in Figure 8 (d). The poor simulation performance may be attributed to two major influencing  
532 factors. First, the location of the heavy rainfall center has a significant impact on the simulation results.  
533 Since the model input uses areal average rainfall, it fails to fully account for the spatial distribution  
534 characteristics of rainfall. As shown in Figure 8(d), when the heavy rainfall center is close to the Shuibuya  
535 Reservoir, the short flow routing time leads to a significant decline in the model simulation performance.  
536 Second, the impact of upstream reservoir regulation cannot be ignored. During multiple flood events in  
537 the Qingjiang River basin in 2020, the Shuibuya Reservoir increased outflow discharge to cope with  
538 severe flood control conditions.

539 All four models underestimated the peak flow discharge, and the simulated peak flow time was  
540 significantly delayed compared to the observed flow peak time. Our study focused on two basins: the  
541 Lushui and Qingjiang River basins. As illustrated in Figure 1, the Qingjiang River basin features a more  
542 complex terrain and a more meandering river network compared to the Lushui River basin. Based on the  
543 flow simulation results shown in Figures 7 and 8, the model performance in the Lushui River basin is  
544 better than that in the Qingjiang River basin. These findings suggest that the model simulation accuracy  
545 in simple terrain basin is higher than that in the complex terrain conditions. For 20201003 and 20200717  
546 flood events, the EDL model's simulated hydrograph was closer to the observed hydrograph compared  
547 to the benchmark models. For 20200628-flood event, the LSTM model performed better during the  
548 recession phase but significantly underestimated the peak flow discharge and failed to accurately  
549 simulate the rising phase. In contrast, the EDL model performed better during the rising and peak phases

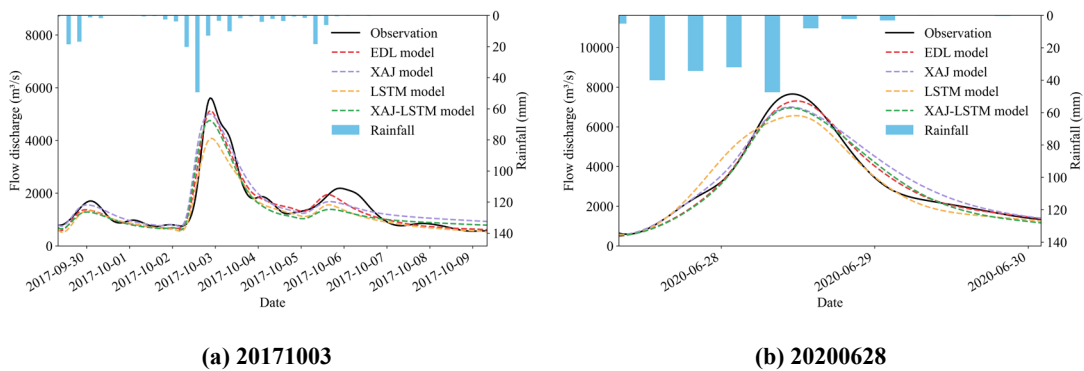
550 but exhibited delays during the recession phase. Overall, although some deviations in peak flow  
 551 discharge and timing exist, the EDL model still effectively captures the general flood trends in the  
 552 Qingjiang River basin.

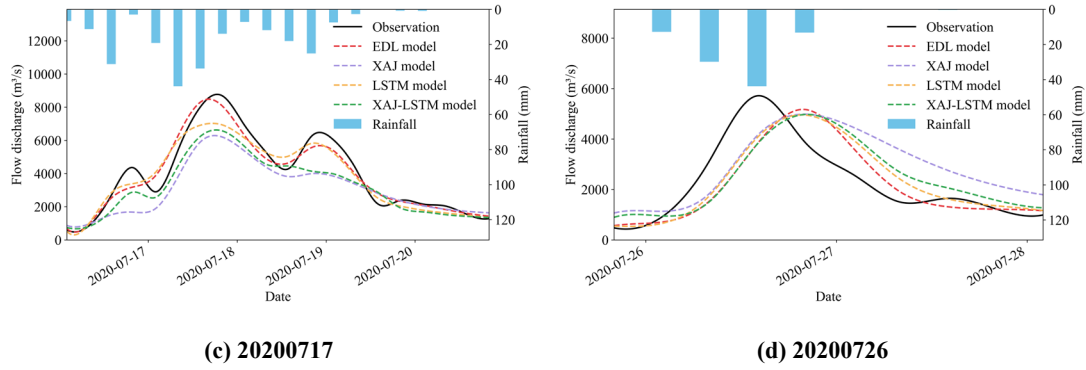
553



554 **Figure 7: Comparison of observed and simulated flood hydrographs in the Lushui River basin.**

555





556 **Figure 8: Comparison of observed and simulated flood hydrographs in the Qingjiang River basin.**

557 **5 Discussion**

558 The XAJ model is a well-established hydrological model utilized for generalizing hydrological  
 559 processes in a basin, including runoff generation and routing. However, when used in isolation, the model  
 560 may struggle to adequately capture intricate nonlinear relationships, particularly evident in flood peak  
 561 simulating where it might not fully account for the impacts of real-time meteorological changes. On the  
 562 other hand, DL models, especially time-series models like LSTM, are adept at capturing complex  
 563 nonlinear relationships within time series data. Nevertheless, they may encounter delays in accurately  
 564 simulating flood peak timings (Chen et al., 2022; Cui et al., 2021; Xiang et al., 2024). To address this  
 565 limitation, a fusion of the XAJ model and DL models can mitigate the weaknesses inherent in each  
 566 approach. Specifically, the conventional hydrological model offers a foundation for physical processes  
 567 that enhance the simulation of basin hydrological responses, while the DL model can refine the output  
 568 of the hydrological model, particularly in terms of temporal accuracy and the comprehension of nonlinear  
 569 relationships. This hybrid approach allows the XAJ model to capture long-term dependencies in  
 570 hydrological processes while enabling the DL model to make more accurate simulations regarding flood  
 571 peak timing, thus effectively minimizing delays in flood peak time.

572 In traditional processes, DL models such as LSTM are commonly employed as post-processors to  
 573 correct the outputs of hydrological models (Cho and Kim, 2022; Cui et al., 2021; Frame et al., 2021; Han  
 574 and Morrison, 2022). Nevertheless, a significant drawback of this methodology stems from the  
 575 inconsistent parameter optimization. Typically, the parameters of the hydrological model are initially  
 576 calibrated to achieve the best simulation results, followed by the training of an LSTM model for

---

577 refinement. Since the parameter adjustments of the hydrological and DL models are conducted  
578 independently, the resulting parameter combination is often suboptimal, thereby constraining simulation  
579 accuracy. A comparison between the EDL model and the XAJ-LSTM model highlights this issue. The  
580 XAJ-LSTM model, which uses the outputs of the traditional XAJ model as inputs and is trained  
581 independently, shows some improvement over the XAJ model but still underperforms compared with the  
582 EDL model. By contrast, the proposed EDL model integrates hydrological and DL components within a  
583 unified framework, enabling synchronized training and joint parameter optimization. This online strategy  
584 not only eliminates the parameter mismatch inherent in conventional post-processing methods but also  
585 ensures that both hydrological and DL parameters are optimized simultaneously, leading to generate  
586 synergistic benefits.

587 This study demonstrates that the proposed EDL model, which tightly integrates physical  
588 mechanisms with DL, can effectively improve the accuracy of flood simulation and forecasting. A  
589 limitation of the present work is that the model parameters were obtained separately for each basin.  
590 Consequently, the current implementation represents a locally trained model that is functionally similar  
591 to traditional calibration. Future research should therefore pursue two complementary directions to  
592 improve generality and adaptability. One is to develop multi-basin (regional or global) training strategies  
593 via differentiable parameter learning, transfer learning, or meta-learning, which can leverage data from  
594 many basins to produce a single, generalizable model. Another is to introduce mechanisms for dynamic,  
595 input-dependent parameter adaptation so that model parameters can evolve with temporal changes in  
596 inputs. Additional promising avenues include explicit uncertainty quantification, tighter coupling  
597 between physics and data-driven components, and online-updating for real-time forecasting. Pursuing  
598 these directions would increase the model applicability across diverse basins and enhance its potential  
599 for scientific discovery.

## 600 **6 Conclusions**

601 The present study proposes a novel EDL model that combines the physics-driven XAJRNN layer  
602 with the LSTM layer, successfully achieving accurate simulation of flood processes in the Lushui River

---

603 basin and Qingjiang River basin. This model leverages the relatively complex physical mechanisms of  
604 the XAJ model and the nonlinear representation capabilities of DL, demonstrating strong simulation  
605 performance. The key findings of this study are as summarized as follows:

606 (1) The EDL model demonstrates superior performance in both simulation accuracy and error  
607 control. It achieves an average *NSE* of 0.98 in the Lushui River basin and 0.94 in the Qingjiang River  
608 basin, demonstrating its outstanding fitting capability. Its average *RMSE* is 38.91 m<sup>3</sup>/s in the Lushui River  
609 basin and 136.02 m<sup>3</sup>/s in the Qingjiang River basin, significantly lower than that of benchmark models,  
610 highlighting its superior simulation accuracy. Although the *RE* is slightly higher during the testing phase,  
611 the combined analysis of the training phase *RE* shows that the EDL model consistently outperforms its  
612 counterparts with stable error control.

613 (2) The EDL model demonstrates the highest stability in most flood simulations. Compared to the  
614 benchmark models, the EDL model achieves smaller *PRE* values, indicating its superior accuracy in  
615 simulating flood peak magnitudes. Moreover, except for a few rare cases, the EDL model's  $\Delta T$  is nearly  
616 zero, showcasing its unparalleled precision in simulating the timing of flood peaks.

617 (3) Compared to traditional single models, the EDL model not only significantly improves  
618 simulation accuracy but also enhances interpretability by integrating physical mechanisms. This  
619 innovative approach paves the way for the seamless integration of DL with hydrological physical  
620 mechanisms, advancing research in the field.

#### 621 **Code availability**

622 The code used to support the findings of this study are available from the corresponding author upon  
623 request.

#### 624 **Data availability**

625 The data generated and/or analyzed during the current study are not publicly available for legal/ethical  
626 reasons but are available from the corresponding author on reasonable request.

---

627 **Author contributions**

628 X.X. and S.G. conceived and designed the experiments; X.X. performed the experiments and wrote the  
629 manuscript draft; X.X., S.G., C.L., and Y.W. reviewed and edited the manuscript.

630 **Competing interests**

631 The authors declare that they have no conflict of interest.

632 **Acknowledgments**

633 This study was financially supported by the National Natural Science Foundation of China (No.  
634 U2340205). The authors would like to thank the editor and anonymous reviewers whose comments and  
635 suggestions help to improve the manuscript.

636 **Appendix A. Supplementary tables and texts**

637 Table A1 describes the state variables of the XAJ model.

638 Table A2 describes the flux of the XAJ model.

639 Table A3 describes parameters and their value ranges of the XAJ model.

640 Table A4 describes the pseudocode of the XAJRNN layer.

641 Text A1 describes the details of the XAJ model.

642

643 **Table A1 State variables of the XAJ model.**

Module	State variable	Meaning	Unit
Evapotranspiration	$W_u$	Areal mean tension water storage of the upper soil layer	mm
	$W_l$	Areal mean tension water storage of the lower soil layer	
	$W_d$	Areal mean tension water storage of the deep soil layer	
Runoff separation	$S_0$	Areal mean free water storage	
Flow routing	$O_i$	Water storage of the interflow linear reservoir	
	$O_g$	Water storage of the groundwater linear reservoir	
	$F_1$	Water storage of the first reservoir in the Nash unit hydrograph	
	$F_2$	Water storage of the second reservoir in the Nash unit hydrograph	
	$F_3$	Water storage of the third reservoir in the Nash unit hydrograph	

644

Table A2 Flux of the XAJ model.

Module	Flux	Meaning	Unit
Evapotranspiration	$P_{obs}$	Areal mean rainfall	
	$E_{obs}$	Measured pan evaporation	
	$P$	Areal mean rainfall of the impervious area	
	$R_{imp}$	Runoff directly from the impervious area	
	$P_n$	Areal mean net rainfall	$mm/\Delta t$
	$E_p$	Potential evapotranspiration	
	$E_u$	Actual evapotranspiration of the upper soil layer	
	$E_l$	Actual evapotranspiration of the lower soil layer	
	$E_d$	Actual evapotranspiration of the deep soil layer	
Runoff generation	$E_t$	Actual evapotranspiration	
	$R$	Runoff produced from the previous area	$mm/\Delta t$
Runoff separation	$R_s$	Surface runoff	
	$R_i$	Interflow runoff	$mm/\Delta t$
	$R_g$	Groundwater runoff	
Flow routing	$Q_i$	Outflow of the interflow linear reservoir	
	$Q_g$	Outflow of the groundwater linear reservoir	
	$Q_t$	Total inflow to channel network	
	$Q_1$	Outflow of the first reservoir in the Nash unit hydrograph	$mm/\Delta t$
	$Q_2$	Outflow of the second reservoir in the Nash unit hydrograph	
	$Q_3$	Outflow of the third reservoir in the Nash unit hydrograph	
	$Q$	Outflow discharge of the basin	$m^3/s$



**Table A3 Parameters and their value ranges of the XAJ model.**

Module	Parameter	Meaning	Value range	Unit
Evapotranspiration	$K_c$	Ratio of potential evapotranspiration to pan evapotranspiration	[0.6,1.5]	-
	$c$	Coefficient of deep evapotranspiration	[0.01,0.2]	-
	$W_{um}$	Areal mean tension water capacity of the upper soil layer	[5,30]	mm
	$W_{lm}$	Areal mean tension water capacity of the lower soil layer	[60,90]	mm
	$W_{dm}$	Areal mean tension water capacity of the deep soil layer	[15,60]	mm
	$A_{imp}$	Ratio of the impervious area	[0.01,0.2]	-
Runoff generation	$b$	Exponent of the tension water capacity curve	[0.1,0.4]	-
Runoff separation	$S_m$	Areal mean of the free water capacity of the surface soil layer	[10,50]	mm
	$ex$	Exponent of the free water capacity curve	[1,1.5]	-
	$K_i$	Outflow coefficient of the free water storage to interflow	[0.1,0.55]	-
	$K_g$	Outflow coefficient of the free water storage to groundwater	[0.7- $K_i$ ]	-
Flow routing	$c_i$	Recession constant of interflow storage	[0.1,0.9]	-
	$c_g$	Recession constant of groundwater storage	[0.9,0.988]	-
	$K_f$	Storage-discharge coefficient of the linear reservoir in the Nash unit hydrograph	[0.1,10]	-

**Algorithm:** the XAJRNN unit

**Input:** Sequences of observed rainfall  $\{P_{obs}\}$  and observed evapotranspiration  $\{E_{obs}\}$

**State initialization:**  $W_u^{(0)} = 0$ ,  $W_l^{(0)} = 0$ ,  $W_d^{(0)} = 0$ ,  $S_0^{(0)} = 0$ ,  $O_i^{(0)} = 0$ ,  $O_g^{(0)} = 0$ ,  $O_s^{(0)} = 0$ ,  $F_1^{(0)} = 0$ ,  $F_2^{(0)} = 0$  and  $F_3^{(0)} = 0$

**Parameters:**  $K_c$ ,  $c$ ,  $W_{um}$ ,  $W_{lm}$ ,  $W_{dm}$ ,  $A_{imp}$ ,  $b$ ,  $S_m$ ,  $ex$ ,  $K_i$ ,  $K_g$ ,  $c_i$ ,  $c_g$ ,  $K_f$ ,  $n$

**function** step\_function ( $[P^{(i)}, E^{(i)}]$ ,  $[W_u^{(i-1)}, W_l^{(i-1)}, W_d^{(i-1)}, S_0^{(i-1)}, O_i^{(i-1)}, O_g^{(i-1)}, O_s^{(i-1)},$

$F_1^{(i-1)}, F_2^{(i-1)}, F_3^{(i-1)}]$ , parameters):

Calculate  $R^{(i)}$ ,  $R_{imp}^{(i)}$ ,  $E_t^{(i)}$ ,  $P_n^{(i)}$ ,  $W_u^{(i)}$ ,  $W_l^{(i)}$ ,  $W_d^{(i)}$  via Eqs. (A1) – (A20)

Calculate  $R_s^{(i)}$ ,  $R_i^{(i)}$ ,  $R_g^{(i)}$ ,  $S_0^{(i)}$  via Eqs. (A21) – (A26)

Calculate  $Q_i^{(i)}$ ,  $Q_g^{(i)}$ ,  $Q_t^{(i)}$ ,  $O_i^{(i)}$ ,  $O_g^{(i)}$  via Eqs. (A27) – (A29)

Calculate  $Q_1^{(i)}$ ,  $Q_2^{(i)}$ ,  $Q_3^{(i)}$ ,  $F_1^{(i)}$ ,  $F_2^{(i)}$ ,  $F_3^{(i)}$  via Eqs. (A30) – (A32)

**return**  $W_u^{(i)}$ ,  $W_l^{(i)}$ ,  $W_d^{(i)}$ ,  $S_0^{(i)}$ ,  $O_i^{(i)}$ ,  $O_g^{(i)}$ ,  $O_s^{(i)}$ ,  $F_1^{(i)}$ ,  $F_2^{(i)}$  and  $F_3^{(i)}$

**do** RNN (step function,  $[\{P\}, \{E\}]$ ,  $[W_u^{(0)}, W_l^{(0)}, W_d^{(0)}, S_0^{(0)}, O_i^{(0)}, O_g^{(0)}, O_s^{(0)}, F_1^{(0)}, F_2^{(0)}, F_3^{(0)}]$ )

to obtain sequences of  $\{W_u\}$ ,  $\{W_l\}$ ,  $\{W_d\}$ ,  $\{S_0\}$ ,  $\{O_i\}$ ,  $\{O_g\}$ ,  $\{O_s\}$ ,  $\{F_1\}$ ,  $\{F_2\}$ ,  $\{F_3\}$

Calculate sequence of  $\{Q\}$  via Eq. (A33)

**Output:** The sequence of runoff at the catchment outlet  $\{Q\}$

651 **Text A1**

652 In the evapotranspiration, considering the uneven vertical distribution of soil, the XAJ model  
653 divides the soil into three layers and calculates the actual evapotranspiration using a three-layer soil  
654 moisture model. The calculation principle is as follows: The upper layer evaporates according to its  
655 evapotranspiration capacity. When the upper layer's water content is insufficient, the remaining  
656 evapotranspiration capacity is supplied by evaporation from the lower layers. The evaporation from the  
657 lower layers is proportional to the water storage in those layers. The ratio of the evaporation from the  
658 lower layer to the remaining evapotranspiration capacity must not be less than the coefficient of deep  
659 evapotranspiration ( $c$ ). Otherwise, the lower layer water storage will supply the insufficient portion. If  
660 the lower layer water storage is not sufficient to compensate, the deep layer water storage will provide  
661 the remainder. The calculation formula is as follows:

$$662 \quad P = P_{obs}(1 - A_{imp}) \quad (A1)$$

$$663 \quad R_{imp} = P_{obs} \times A_{imp}$$

$$664 \quad E_p = K_c E_{obs} \quad (A2)$$

665 (1) When  $W_u + P \geq E_p$ ,

$$666 \quad E_u = E_p; E_l = 0; E_d = 0 \quad (A2)$$

667 (2) When  $W_u + P < E_p$  and  $W_l \geq c \times W_{lm}$ ,

$$668 \quad E_u = W_u + P; E_l = (E_p - E_u) \times W_l / W_{lm}; E_d = 0 \quad (A3)$$

669 (3) When  $W_u + P < E_p$  and  $c \times (E_p - E_u) \leq W_l < c \times W_{lm}$ ,

$$670 \quad E_u = W_u + P; E_l = c \times (E_p - E_u); E_d = 0 \quad (A4)$$

671 (4) When  $W_u + P < E_p$  and  $c \times (E_p - E_u) > W_l$ ,

$$672 \quad E_u = W_u + P; E_l = W_l; E_d = c \times (E_p - E_u) - E_l \quad (A5)$$

$$673 \quad E_t = E_u + E_l + E_d \quad (A6)$$

$$674 \quad P_n = \begin{cases} P - E_t, & P \geq E_t \\ 0, & P < E_t \end{cases} \quad (A7)$$

675 The runoff generation calculation uses the tension water capacity curve. First, it is necessary to  
676 calculate the areal mean tension water storage ( $W$ ) and the areal mean tension water capacity ( $W_m$ ):

$$677 \quad W = W_u + W_l + W_d \quad (A8)$$

$$678 \quad W_m = W_{um} + W_{lm} + W_{dm} \quad (A9)$$

679 The vertical coordinate value ( $\alpha$ ) corresponding to the areal mean tension water storage ( $W$ ) on the  
 680 tension water capacity curve is calculated as:

$$681 \quad \alpha = W_m \times (b + 1) \times \left[ 1 - \left( 1 - \frac{W}{W_m} \right)^{\frac{1}{1+b}} \right] \quad (\text{A11})$$

682 Calculate the runoff produced from the previous area:

$$683 \quad R = \begin{cases} P_n + W - W_m + W_m \left( 1 - \frac{P_n + \alpha}{W_m \times (b+1)} \right)^{b+1}, & P_n + \alpha \leq W_m \times (b + 1) \\ P_n + W - W_m, & P_n + \alpha > W_m \times (b + 1) \end{cases} \quad (\text{A12})$$

684 Finally, update the areal mean tension water storage of the upper, lower, and deep soil layer of the  
 685 watershed at the end of the current period, which will serve as the initial values for the next period:

$$686 \quad W_u = W_u + P - E_t - R \quad (\text{A13})$$

$$687 \quad W_l = W_l - E_l \quad (\text{A14})$$

$$688 \quad W_d = \max(W_d - E_d, 0) \quad (\text{A15})$$

689 When  $W_u > W_{um}$ ,

$$690 \quad W_l = W_l + W_u - W_{um} \quad (\text{A16})$$

$$691 \quad W_u = W_{um} \quad (\text{A17})$$

692 When  $W_l > W_{lm}$ ,

$$693 \quad W_d = W_d + W_l - W_{lm} \quad (\text{A18})$$

$$694 \quad W_l = W_{lm} \quad (\text{A19})$$

$$695 \quad W_d = \min(W_d, W_{dm}) \quad (\text{A20})$$

696 The runoff separation uses the free water capacity curve. The vertical coordinate value ( $\beta$ )  
 697 corresponding to the areal mean free water storage ( $S_0$ ) is:

$$698 \quad \beta = S_m \times (ex + 1) \times \left[ 1 - \left( 1 - S_0/S_m \right)^{\frac{1}{1+ex}} \right] \quad (\text{A21})$$

699 Therefore, the surface runoff ( $R_s$ ) is:

$$700 \quad R_s = \begin{cases} R + \left\{ S_0 - S_m + S_m \left[ 1 - \frac{(P_n + \beta)}{S_m \times (ex+1)} \right]^{ex+1} \right\} \frac{R}{P_n}, & P_n + \beta \leq S_m \times (ex + 1) \\ R + (S_0 - S_m) \frac{R}{P_n}, & P_n + \beta > S_m \times (ex + 1) \end{cases} \quad (\text{A22})$$

$$701 \quad R_s = R_s + R_{imp} \quad (\text{A23})$$

702 The interflow runoff ( $R_i$ ):

$$703 \quad R_i = K_i \times S_0 \times \frac{R}{P_n} \quad (\text{A24})$$

704 The groundwater runoff ( $R_g$ ):

---

705 
$$R_g = K_g \times S_0 \times \frac{R}{P_n} \quad (A25)$$

706 Calculate the areal mean free water storage ( $S_0$ ) at the end of the current period, which will serve as  
 707 the initial value for the next period, as:

708 
$$S_0 = S_0 + (R - R_s - R_i - R_g) \times \frac{P_n}{R} \quad (A26)$$

709 The flow routing module consists of two submodules: hillslope and channel network routing. The  
 710 hillslope routing adopts a linear reservoir approach, while the channel network routing uses the Nash unit  
 711 hydrograph. The calculation formula for the linear reservoir is as follows:

712 
$$Q_i = -O_i \times \ln c_i \quad (A27)$$

713 
$$Q_g = -O_g \times \ln c_g \quad (A28)$$

714 The total inflow to channel network is equal to the sum of the surface runoff ( $R_s$ ), the outflow of  
 715 the interflow linear reservoir ( $Q_i$ ), and the outflow of the groundwater linear reservoir ( $Q_g$ ). The  
 716 calculation formula is as follows:

717 
$$Q_t = R_s + Q_i + Q_g \quad (A29)$$

718 The calculation formula for the Nash unit hydrograph reservoir is as follows:

719 
$$Q_1 = F_1/K_f \quad (A30)$$

720 
$$Q_2 = F_2/K_f \quad (A31)$$

721 
$$Q_3 = F_3/K_f \quad (A32)$$

722 The calculation formula for the outflow discharge of the basin ( $Q$ ) is as follows:

723 
$$Q = Q_3 \times 1000 \times F/\Delta t \quad (A33)$$

724 where  $F$  is the watershed area,  $\text{km}^2$ .  $\Delta t$  is the input time step, s.

---

725 **Reference**

- 726 Alizadeh, B., Ghaderi Bafti, A., Kamangir, H., Zhang, Y., Wright, D. B., and Franz, K. J.: A novel  
727 attention-based LSTM cell post-processor coupled with Bayesian optimization for streamflow  
728 prediction, *J. Hydrol.*, 601, 126526, <https://doi.org/10.1016/j.jhydrol.2021.126526>, 2021.
- 729 Bindas, T., Tsai, W., Liu, J., Rahmani, F., Feng, D., Bian, Y., Lawson, K., and Shen, C.: Improving river  
730 routing using a differentiable Muskingum-Cunge model and physics-informed machine learning,  
731 *Water Resour. Res.*, 60, e2023WR035337, <https://doi.org/10.1029/2023WR035337>, 2024.
- 732 Boucher, M. A., Quilty, J., and Adamowski, J.: Data assimilation for streamflow forecasting using  
733 extreme learning machines and multilayer perceptrons, *Water Resour. Res.*, 56, e2019WR026226,  
734 <https://doi.org/10.1029/2019WR026226>, 2020.
- 735 Chen, C., Jiang, J., Liao, Z., Zhou, Y., Wang, H., and Pei, Q.: A short-term flood prediction based on  
736 spatial deep learning network: A case study for Xi County, China, *J. Hydrol.*, 607, 127535,  
737 <https://doi.org/10.1016/j.jhydrol.2022.127535>, 2022.
- 738 Cheng, C., Zhao, M., Chau, K. W., and Wu, X.: Using genetic algorithm and TOPSIS for Xinanjiang  
739 model calibration with a single procedure, *J. Hydrol.*, 316, 129–140,  
740 <https://doi.org/10.1016/j.jhydrol.2005.04.022>, 2006.
- 741 Cho, K. and Kim, Y.: Improving streamflow prediction in the WRF-Hydro model with LSTM networks,  
742 *J. Hydrol.*, 605, 127297, <https://doi.org/10.1016/j.jhydrol.2021.127297>, 2022.
- 743 Cui, Z., Zhou, Y., Guo, S., Wang, J., Ba, H., and He, S.: A novel hybrid XAJ-LSTM model for multi-  
744 step-ahead flood forecasting, *Hydrol. Res.*, 52, 1436–1454, <https://doi.org/10.2166/nh.2021.016>,  
745 2021.
- 746 De la Fuente, L. A., Ehsani, M. R., Gupta, H. V., and Condon, L. E.: Toward interpretable LSTM-based  
747 modeling of hydrological systems, *Hydrol. Earth Syst. Sci.*, 28, 945–971,  
748 <https://doi.org/10.5194/hess-28-945-2024>, 2024.
- 749 Feng, D., Liu, J., Lawson, K., and Shen, C.: Differentiable, learnable, regionalized process-based models  
750 with multiphysical outputs can approach state-of-the-art hydrologic prediction accuracy, *Water*  
751 *Resour. Res.*, 58, e2022WR032404, <https://doi.org/10.1029/2022WR032404>, 2022.
- 752 Feng, D., Beck, H., Lawson, K., and Shen, C.: The suitability of differentiable, physics-informed machine  
753 learning hydrologic models for ungauged regions and climate change impact assessment, *Hydrol.*  
754 *Earth Syst. Sci.*, 27, 2357–2373, <https://doi.org/10.5194/hess-27-2357-2023>, 2023.
- 755 Frame, J. M., Kratzert, F., Raney II, A., Rahman, M., Salas, F. R., and Nearing, G. S.: Post-processing  
756 the national water model with long short-term memory networks for streamflow predictions and  
757 model diagnostics, *J. Am. Water Resour. Assoc.*, 57, 885–905, <https://doi.org/10.1111/1752-1688.12964>, 2021.
- 759 Frame, J. M., Kratzert, F., Gupta, H. V., Ullrich, P., and Nearing, G. S.: On strictly enforced mass  
760 conservation constraints for modelling the Rainfall-Runoff process, *Hydrol. Process.*, 37, e14847,  
761 <https://doi.org/10.1002/hyp.14847>, 2023.
- 762 Frank, E. S., Zhen, Y., Han, F., Shailesh, T., and Matthias, D.: An introductory review of deep learning  
763 for prediction models with big data, *Front. Artif. Intell.*, 3, 4,  
764 <https://doi.org/10.3389/frai.2020.00004>, 2020.
- 765 Guido, B. I., Popescu, I., Samadi, V., and Bhattacharya, B.: An integrated modeling approach to evaluate

---

766 the impacts of nature-based solutions of flood mitigation across a small watershed in the southeast  
767 United States, *Nat. Hazard. Earth Sys.*, 23, 2663–2681, <https://doi.org/10.5194/nhess-23-2663-2023>,  
768 2023.

769 Han, H. and Morrison, R. R.: Improved runoff forecasting performance through error predictions using  
770 a deep-learning approach, *J. Hydrol.*, 608, 127653, <https://doi.org/10.1016/j.jhydrol.2022.127653>,  
771 2022.

772 He, L., Shi, L., Song, W., Shen, J., Wang, L., Hu, X., and Zha, Y.: Synergizing intuitive physics and big  
773 data in deep learning: Can we obtain process insights while maintaining state-of-the-art hydrological  
774 prediction capability? *Water Resour. Res.*, 60, e2024WR037582,  
775 <https://doi.org/10.1029/2024WR037582>, 2024.

776 Hirabayashi, Y., Mahendran, R., Koirala, S., Konoshima, L., Yamazaki, D., Watanabe, S., Kim, H., and  
777 Kanae, S.: Global flood risk under climate change, *Nat. Clim. Chang.*, 3, 816–821,  
778 <https://doi.org/10.1038/nclimate1911>, 2013.

779 Hochreiter, S. and Schmidhuber, J.: Long short-term memory, *Neural Comput.*, 9, 1735–1780,  
780 <https://doi.org/10.1162/neco.1997.9.8.1735>, 1997.

781 Hoedt, P. J., Kratzert, F., Klotz, D., Halmich, C., Holzleitner, M., Nearing, G., Hochreiter, S., and  
782 Klambauer, G.: MC-LSTM: Mass-conserving LSTM, in: *Proceedings of Machine Learning  
783 Research, Proceedings of the 38th International Conference on Machine Learning, San Diego, Web  
784 of Science ID: WOS:000683104604027*, 2021.

785 Jiang, S., Zheng, Y., and Solomatine, D.: Improving AI system awareness of geoscience knowledge:  
786 Symbiotic integration of physical approaches and deep learning, *Geophys. Res. Lett.*, 47,  
787 e2020GL088229, <https://doi.org/10.1029/2020GL088229>, 2020.

788 La Follette, P. T., Teuling, A. J., Addor, N., Clark, M., Jansen, K., and Melsen, L. A.: Numerical demons  
789 of hydrological models are summoned by extreme precipitation, *Hydrol. Earth Syst. Sci.*, 25, 5425–  
790 5446, <https://doi.org/10.5194/hess-25-5425-2021>, 2021.

791 Li, H., Zhang, C., Chu, W., Shen, D., and Li, R.: A process-driven deep learning hydrological model for  
792 daily rainfall-runoff simulation, *J. Hydrol.*, 637, 131434,  
793 <https://doi.org/10.1016/j.jhydrol.2024.131434>, 2024.

794 Li, Z., Kan, G., Yao, C., Liu, Z., Li, Q., and Yu, S.: Improved neural network model and its application  
795 in hydrological simulation, *J. Hydrol. Eng.*, 19, 04014019,  
796 [https://doi.org/10.1061/\(ASCE\)HE.1943-5584.0000958](https://doi.org/10.1061/(ASCE)HE.1943-5584.0000958), 2014.

797 Nash, J. E. and Sutcliffe, J. V.: River flow forecasting through conceptual models part I - A discussion of  
798 principles, *J. Hydrol.*, 10, 282–290, [https://doi.org/10.1016/0022-1694\(70\)90255-6](https://doi.org/10.1016/0022-1694(70)90255-6), 1970.

799 Nearing, G. S., Kratzert, F., Sampson, A. K., Pelissier, C. S., Klotz, D., Frame, J. M., Prieto, C., and  
800 Gupta, H. V.: What role does hydrological science play in the age of machine learning? *Water Resour.  
801 Res.*, 57, e2020WR028091, <https://doi.org/10.1029/2020WR028091>, 2021.

802 Niu, M. Y., Horesh, L., and Chuang, I.: Recurrent neural networks in the eye of differential equations,  
803 <https://doi.org/10.48550/arXiv.1904.12933>, 29 April 2019.

804 Pokharel, S., Roy, T., and Admiraal, D.: Effects of mass balance, energy balance, and storage-discharge  
805 constraints on LSTM for streamflow prediction, *Environ. Modell. Softw.*, 166, 105730,  
806 <https://doi.org/10.1016/j.envsoft.2023.105730>, 2023.

807 Roy, A., Kasiviswanathan, K. S., Patidar, S., Adeloye, A. J., Soundharajan, B. S., and Ojha, C. S. P.: A

---

808 physics-aware machine learning-based framework for minimizing prediction uncertainty of  
809 hydrological models, *Water Resour. Res.*, 59, e2023WR034630,  
810 <https://doi.org/10.1029/2023WR034630>, 2023.

811 Rumelhart, D. E., Hinton, G. E., and Williams, R. J.: Learning representations by back-propagating errors,  
812 *Nature*, 323, 533–536, <https://doi.org/10.1038/323533a0>, 1986.

813 Shen, C.: A transdisciplinary review of deep learning research and its relevance for water resources  
814 scientists, *Water Resour. Res.*, 54, 8558–8593, <https://doi.org/10.1029/2018WR022643>, 2018.

815 Shen, C., Appling, A. P., Gentine, P., Bandai, T., Gupta, H., Tartakovsky, A., Baity-Jesi, M., Fenicia, F.,  
816 Kifer, D., Li, L., Liu, X., Ren, W., Zheng, Y., Harman, C. J., Clark, M., Farthing, M., Feng, D.,  
817 Kumar, P., Aboelyazeed, D., Rahmani, F., Song, Y., Beck, H. E., Bindas, T., Dwivedi, D., Fang, K.,  
818 Höge, M., Rackauckas, C., Mohanty, B., Roy, T., Xu, C., and Lawson, K.: Differentiable modelling  
819 to unify machine learning and physical models for geosciences, *Nat. Rev. Earth Environ.*, 4, 552–  
820 567, <https://doi.org/10.1038/s43017-023-00450-9>, 2023.

821 Singh, V. P.: Estimation of parameters of a uniformly nonlinear surface runoff model, *Hydrol. Res.*, 8,  
822 33–46, <https://doi.org/10.2166/nh.1977.0003>, 1977.

823 Song, Y., Knoben, W. J. M., Clark, M. P., Feng, D., Lawson, K., Sawadekar, K., and Shen, C.: When  
824 ancient numerical demons meet physics-informed machine learning: adjoint-based gradients for  
825 implicit differentiable modeling, *Hydrol. Earth Syst. Sci.*, 28, 3051–3077,  
826 <https://doi.org/10.5194/hess-28-3051-2024>, 2024.

827 Thaisiam, W., Yomwilai, K., and Wongchaisuwat, P.: Utilizing sequential modeling in collaborative  
828 method for flood forecasting, *J. Hydrol.*, 636, 131290,  
829 <https://doi.org/10.1016/j.jhydrol.2024.131290>, 2024.

830 Tsai, W. P., Feng, D., Pan, M., Beck, H., Lawson, K., Yang, Y., Liu, J., and Shen, C.: From calibration to  
831 parameter learning: Harnessing the scaling effects of big data in geoscientific modeling, *Nat.*  
832 *Commun.*, 12, 5988, <https://doi.org/10.1038/s41467-021-26107-z>, 2021.

833 Wang, C., Jiang, S., Zheng, Y., Han, F., Kumar, R., Rakovec, O., and Li, S.: Distributed hydrological  
834 modeling with physics-encoded deep learning: A general framework and its application in the  
835 Amazon, *Water Resour. Res.*, 60, e2023WR036170, <https://doi.org/10.1029/2023WR036170>, 2024.

836 Wang, N., Zhang, D., Chang, H., and Li, H.: Deep learning of subsurface flow via theory-guided neural  
837 network, *J. Hydrol.*, 584, 124700, <https://doi.org/10.1016/j.jhydrol.2020.124700>, 2020.

838 Wang, Y.-H. and Gupta, H. V.: Towards interpretable physical-conceptual catchment-scale hydrological  
839 modeling using the mass-conserving-perceptron, *Water Resour. Res.*, 60, e2024WR037224,  
840 <https://doi.org/10.1029/2024WR037224>, 2024.

841 Worland, S. C., Steinschneider, S., Asquith, W., Knight, R., and Wiczorek, M.: Prediction and inference  
842 of flow duration curves using multioutput neural networks, *Water Resour. Res.*, 55, 6850–6868,  
843 <https://doi.org/10.1029/2018WR024463>, 2019.

844 Xiang, X., Guo, S., Cui, Z., Wang, L., and Xu, C. Y.: Improving flood forecast accuracy based on  
845 explainable convolutional neural network by Grad-CAM method, *J. Hydrol.*, 642, 131867,  
846 <https://doi.org/10.1016/j.jhydrol.2024.131867>, 2024.

847 Xie, K., Liu, P., Zhang, J., Han, D., Wang, G., and Shen, C.: Physics-guided deep learning for rainfall-  
848 runoff modeling by considering extreme events and monotonic relationships, *J. Hydrol.*, 603,  
849 127043, <https://doi.org/10.1016/j.jhydrol.2021.127043>, 2021.



---

850 Xu, Y., Hu, C., Wu, Q., Jian, S., Li, Z., Chen, Y., Zhang, G., Zhang, Z., and Wang, S.: Research on particle  
851 swarm optimization in LSTM neural networks for rainfall-runoff simulation, *J. Hydrol.*, 608,  
852 127553, <https://doi.org/10.1016/j.jhydrol.2022.127553>, 2022.

853 Yang, S., Yang, D., Chen, J., Santisirisomboon, J., Lu, W., and Zhao, B.: A physical process and machine  
854 learning combined hydrological model for daily streamflow simulations of large watersheds with  
855 limited observation data, *J. Hydrol.*, 590, 125206, <https://doi.org/10.1016/j.jhydrol.2020.125206>,  
856 2020.

857 Yann, L., Yoshua, B., and Geoffrey, H.: Deep learning, *Nature*, 521, 436–444,  
858 <https://doi.org/10.1038/nature14539>, 2015.

859 Yao, C., Li, Z., Bao, H., and Yu, Z.: Application of a developed grid-Xinjiang model to Chinese  
860 watersheds for flood forecasting purpose, *J. Hydrol. Eng.*, 14, 923–934,  
861 [https://doi.org/10.1061/\(ASCE\)HE.1943-5584.0000067](https://doi.org/10.1061/(ASCE)HE.1943-5584.0000067), 2009.

862 Yao, C., Zhang, K., Yu, Z., Li, Z., and Li, Q.: Improving the flood prediction capability of the Xinjiang  
863 model in ungauged nested catchments by coupling it with the geomorphologic instantaneous unit  
864 hydrograph, *J. Hydrol.*, 517, 1035–1048, <https://doi.org/10.1016/j.jhydrol.2014.06.037>, 2014.

865 Zhao, R.: The Xinjiang model applied in China, *J. Hydrol.*, 135, 371–381,  
866 [https://doi.org/10.1016/0022-1694\(92\)90096-E](https://doi.org/10.1016/0022-1694(92)90096-E), 1992.

867 Zhao, R.: A non-linear system model for basin concentration, *J. Hydrol.*, 142, 477–482,  
868 [https://doi.org/10.1016/0022-1694\(93\)90024-4](https://doi.org/10.1016/0022-1694(93)90024-4), 1993.

869 Zhong, L., Lei, H., Li, Z., and Jiang, S.: Advancing streamflow prediction in data-scarce regions through  
870 vegetation-constrained distributed hybrid ecohydrological models, *J. Hydrol.*, 645, 132165,  
871 <https://doi.org/10.1016/j.jhydrol.2024.132165>, 2024a.

872 Zhong, L., Lei, H., and Yang, J.: Development of a distributed physics-informed deep learning  
873 hydrological model for data-scarce regions, *Water Resour. Res.*, 60, e2023WR036333,  
874 <https://doi.org/10.1029/2023WR036333>, 2024b.

875 Zhou, Y., Guo, S., Liu, P., and Xu, C.: Joint operation and dynamic control of flood limiting water levels  
876 for mixed cascade reservoir systems, *J. Hydrol.*, 519, 248–257,  
877 <https://doi.org/10.1016/j.jhydrol.2014.07.029>, 2014.

878